Graz University of Technology

Institute of Control and Automation, TU Graz

Institute of cybernetics, NTNU Trondheim

Master's Thesis

NANOPOSITIONING-
IMPROVING RESOLUTION IN CLOSED LOOP POSITION CONTROL

Lukas Vogl

Graz, Austria, February 2010

Thesis supervisors

Ao.Univ.-Prof. Dipl.-Ing. Dr.techn. Michael Hofbaur
Ao.Univ.-Prof. Dipl.-Ing. Dr.techn. Jan Tommy Gravdahl
Dipl.Ing. Arnfinn Aas Eielsen

Abstract

In this thesis the subjects of system analysis and state estimation of a piezoelectric tube actuator are discussed. The considered system can be modelled as an LTI-model in series with a hysteresis differential model. Appropriate models for the hysteresis effect and the tube dynamics are presented. A new state-space representation of the total system combines the aforementioned models. The advantageous properties of a capacitive and strain sensor are employed for displacement measurement.

Under these preconditions, features of a Kalman filter are utilized to fuse the sensor signals in an optimal way. This approach was tested in a real lab setup and resulted in successful measurements. Eventually a simple controller design was used to improve the system performance at higher scanning rates.

Keywords. Piezoelectric tube, Hysteresis model, Kalman filtering, Nonlinear piezoelectric tube model.

Acknowledgments

Eventually I take the last step of my academic education. When I look back, years of joy, years with agitation, years with new countries, years with new experiences and, yes, also years with disappointments lie behind me. Time goes by and new challenges will come but what still remains is the memory of a wonderful time. Many people accompanied me during the past years and believed in me throughout the whole time.

First of all I want to name my parents Ruth and Alois, who supported me in any possible situation. Without their help, care and patience I would not be where I am now. The same applies for my brother and friend Fabian who has always been a loyal partner to me. Special thanks go to my aunts and uncles Helga and Kurt Doller and Herrat and Bernd Vogl for simply everything they did. Furthermore I want to thank Sylvia and Burkhard Vogl for their great support. They gave the word promptness a new definition.

I would like to thank my supervisors, professor Michael Hofbaur and professor Jan Tommy Gravdahl, who made my stay in Trondheim possible. They guided me through the thesis work with great support and help. The same applies for PhD student Arnfinn Aas Eielsen, who gave me invaluable advice and insights in the matter of this thesis. The workshop team at ITK with Terje Haugen and Jon Olav Horrigmo did a great job and backed me up with their great experience.

Special thanks I owe to many student fellows. In first place to be mentioned is my long campaigner Michael Schullin, who I share many wonderful experiences with. My running friend Stefan Laimgruber who helped me with any kind of problem. The same applies to my friend Christoph Gruber and his great support during my unique stay in Trondheim, which would not have been the same without him. Marte-Mari Moen my language partner, who introduced me into the Norwegian way of life. Furthermore I owe great thanks to Georg, Anna, Tord, Andrea, Thomas, Alois and many more.

Thank you, Tack, Danke, Takk!

Contents

List of Figures

List of Tables

Chapter 1

Introduction

1.1 Motivation

In the past a tremendous effort was put into observing materials. Scaling down to hundreds of micrometers was insufficient to meet the today's requirements hence nanometer resolution became necessary for many processes. As conventional optical microscopes are not able to cope with such a task, new methods had to be invented. Binnig (1984) [14] was able to construct the first scanning probe microscope (SPM) which simply scans a sample in a defined raster pattern and measures the current at the related position. Piezoelectric tubes (PZT) have been used as actuators which provide an acceptable scanning range at a decent bandwidth. Over the last couple of years such PZTs were the main interest of ongoing research within SPMs. New control schemes, more exact models, analysis of diverse nonlinearities or implementation of estimation methods are just some of the latest efforts. Continuous progress and improvements of the existing methods promise even better resolution results in the future. Different research groups throughout the world are fascinated by these problems and are actively working on improvements in several fields of operation. At NTNU the groundwork for research within nanometer positioning has been carried out in several projects and is continued by this thesis. The focus is mainly to gain achievements in the area of system modelling and estimation methods for the tube displacement where exact displacement is probably the most important issue for such small deflections. The author's intention is to attain a reliable method which can be used in the future for several projects within nanopositioning at NTNU.

1.2 Contributions of this thesis

This thesis describes a method to improve the resolution of a nanometer positioning system. Based on previous works, a piezoeletric tube actuator was the system of interest. Besides some basic hardware changes, several other attempts were developed to improve the resolution. Measurement circuits were redesigned to obtain less noise with higher precision. A new nonlinear model in state space form is developed to meet the requirements of implementation for both a Kalman filter and a controller. Conducted experiments, circuit design and modelling issues are partly inspired by research done at The University of Newcastle (Australia), The University of Technology, Delft (Netherlands) and the MIT (USA). References to these and others are given were they are relevant. Other articles related to the topic of nanopositioning are given in [28] [2]. Results of this thesis will be compared to actual findings wherever comparison is useful.

1.3 SPM background

Scanning probe microscopes are designed to image objects in the range of nanometers where common optical microscopes become useless. Among several different techniques and types of SPMs, the scanning tunnelling microscope (STM) and the atomic force microscope (AFM) are the most common ones. Areas of science range from cell biology to crystallography, molecular electronics, etc.. Such microscopes are able to depict topographical constellations of solid surfaces down to sub-nanometer resolution. For both microscopes a target or probe is placed in close range to the microscope's tip. The whole area of interest is scanned either by moving the tip or the probe itself.

Within the STM technology the information about the topography is gathered via electron tunnelling from the tip to the probe (this presumes a conductor or semiconductor as a sample material). The STM can be run in two different modes. One possibility is to hold the current at a constant level, which requires a height control of the tip. The control signal of the z-direction then comprises information about the topography. The second possible mode is the constant height mode. With that, the tip height is fixed and the distance between the probe and tip changes. Corresponding to those changes the current flow changes as well. A topographical map can then be constructed out of the changing current flow.

The second type of SPM, an AFM, measures the arising forces between the sample and a cantilever tip by optically evaluating the deflection of the probe. This is typically done by a laser beam pointing on the tip. Several modes of operation are possible while the sample is moved in a raster pattern to obtain an entire surface plot. In contact mode the tip is in direct contact with the sample surface. For the tapping mode, the probe is oscillated to constantly tap the surface. This results in less friction effects and more reliable measurements especially for soft surface scans. Within the non-contact mode the cantilever is oscillated without touching the surface. Weak attractive forces affect the oscillations which result in a frequency change. This change is measured and converted into a figure. (Compare [33],[4] for more detailed information)

1.4 Structure of this document

In Chapter 2 the basic hardware with the sensors in use are explained and possible problems concerning the grounding are emphasised. Chapter 3 deals with system modelling. The whole setup is split into several parts where each is described respectively with a state space model as well as a transfer function. Different appropriate models for nonlinear effects are additionally presented. Chapter 4 consists of the partial models to a model describing the whole system. Both a linear and nonlinear version is discussed. Kalman filtering is introduced and adapted to the system models in Chapter 5. Simulation and experimental results are presented in the following. In Chapter 6 diverse controller realisations for both the linear and nonlinear systems are suggested. Eventually, in Chapter 7 results and investigations from the preceding chapters are summarized and discussed. Conclusions and further work is presented.

Chapter 2

Experimental setup

This chapter presents the setup actually used in the lab. A desired signal is generated on a PC which is connected to a digital/ analogue conversion unit (dSpace). The voltage output is amplified and connected to one of the PZT electrodes. Displacement of the tube is measured by both a capacitive and a strain sensor. An illustration is given in Figure 2.1.

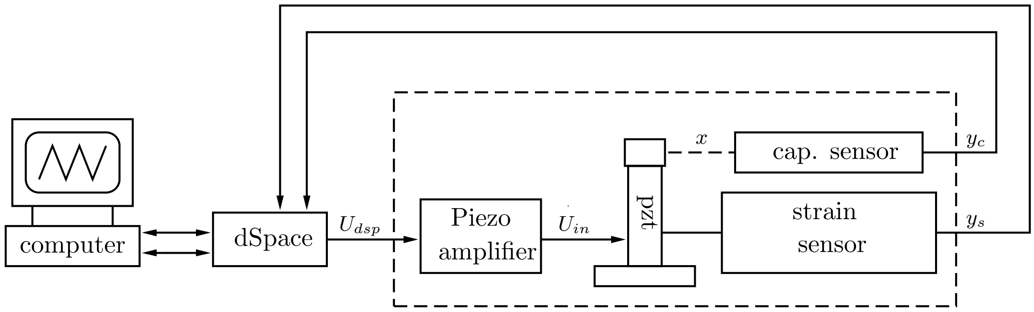

Figure 2.1: Block diagram of the total lab setup

2.1 Hardware

2.1.1 Fixtures

From the basic ideas and implementations of earlier projects [32], the lab hardware was systematically improved and extended. For a more detailed documentation compare also [32]. Of vital importance for precise measurements is a solid construction, which allows minimal vibration but also shields the setup from outer disturbances (noise, vibration).

To meet these requirements the actuator, a piezoelectric tube, is fixed onto an aluminium disc, which moreover is bolted to the base (Figure 2.2(a)). To achieve electrical insulation between the tube and the disc on the one side, but also a firm connection on the other side is a tricky task. The same problem appears in relation to the cube on the top. This problem was handled by using a special glue. As a first step the cube and the disc were bonded separately. The following lathing treatment guaranteed a perfect fit and insulation too. In the second step the insulating planes were bonded onto the tube. Furthermore the setup was placed in a cylindrical enclosure to protect the measurements from additional external noise (Figure 2.2(b)). Capacitive sensors were fixed in the enclosure to measure the cube's deflection. Connecting wires from the electrodes and the cube were led through an outlet to a terminal board. The distance to the plug is kept small, again to minimize external noise. Connection to the separate instruments is realized via 50Ω Coax-cabels.

(a) (b)

Figure 2.2: Piezoelectric tube isolated from the cube and base (a). Piezoeletric tube setup with the capacitive sensors right angled to the cube fixed in the enclosure (b).

2.1.2 Vibration isolation

The microscope setup fixed on a rigid table is a possible realization - but not a good one. External vibrations which can be caused by anything from motors, capacities to building vibrations can lead to a tremendous aggravation in precision performance. Hence it is of great importance to reduce any components causing external vibration. Principally this can be done by two simple actions.

1. The fixtures should have the highest possible resonant frequency
2. Good damping from the surrounding

Actions to meet point 1 are partly discussed in Section 2.1. Concerning point 2 several possibilities can be taken into consideration. Generally, [8] suggested to distinguish between 3 different damping technologies.

1. **Elastomeric rubbers**
   The microscopy setup is placed on a rubber board which should damp surrounding vibrations. Such a method has been used in [32] but led to insufficient measurements.
2. **Air table**
   The usage of an air table improved the measurement performance noticeably and is actually installed in the laboratory.
3. **Active damping**
   A more costly method is active damping where damping is actively affected and damped. This method is not used in the lab. Further information relevant to this can be found in [22].

2.2 Piezoelectric actuator

The piezoelectric actuator in this case is a thin walled tube made from the chemical composition $PbZr_{0.35}Ti_{0.47}O_3$. A schematic drawing is given in Figure 2.3. Both the inside and outside of the tube are coated with a thin layer of nickel. The tube's inside is fully coated whereas the outside is divided into four 90° sections. A pair of opposite electrodes (E_1 and E_3) is accountable for x-displacement whereas y-displacement is referred to the other pair (E_2 and E_4). Deflection can be achieved by driving a pair of electrodes with signals of identical magnitude but opposite signs. Obviously this is linked with a loss of possible strain measurements. Another method to achieve a deflection in the $x-y$ plane is to apply a single voltage to one electrode only (e.g. E_1). Displacement will be less at the benefits of a strain measurement (E_3). Deflection in z-direction can be achieved by applying a voltage to all the outer electrodes or by applying a voltage to the inner electrode E_i (with respect to ground level).

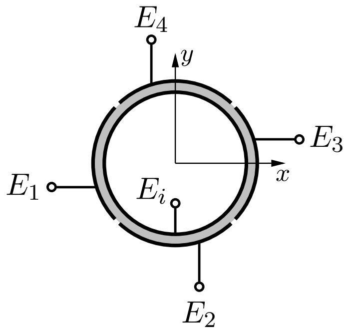

Figure 2.3: Piezoelectric actuator from the top with possible connections.

2.3 Capacitive sensor

2.3.1 Working principle

In nanotechnology capacitive sensing became very popular in the past, mostly due to the simple technique when non-contact measurement is needed. The working principle is based on the movement of the target, which changes the capacity between the fixed sensor and the moving (cube) electrode. With that, a certain capacity matches a certain distance. Evaluation units for such sensors convert the capacity into a voltage, where they then provide an output voltage as a function of the cube's displacement. Usually these units are the most critical part as they have to cope with capacitance variations of less than 0.1fF in order to achieve nanometer position resolution. Considering the presence of possible parasitic capacitance, this part of sensing is probably the most crucial one. Relations as described in Chapter 3 are only valid if the cube is aligned perfectly parallel to the sensor, which happens to be another crucial precision criterion.

2.3.2 Multi-probe setup

In a further stage the laboratory setup should be used in scanning mode. This means both axes are actuated at the same time and the capacitance measurement is coexistent. If the measurement noise shows a minimum in single operation mode (either x- or y-deflection is measured) but an enhanced noise level during $x - y$ measurement tests, the problem of incompatible tuning is present. This means an internal signal from one sensor is disturbing the measurements from the opponent. Observations in the lab showed a 220kHz signal in the noise which comes from the internal signal from the opposite sensor. To still use the capacitance gauging system in a multi-probe setup the sensors need to have different internal frequencies which are separated by at least Δ100kHz.

2.4 Piezoelectric strain sensor

The piezoelectric strain sensor relies on the *direct piezoelectric effect*. This effect, first discovered by the Curie brothers (1883), describes the ability of materials to generate an electric potential when they are under mechanical stress or pressure. In the same way piezoelectric materials (notably crystals and certain ceramics) can be deformed by applying a certain voltage to the material. Depending on the sign the material is contracted or expanded. In related literature [15] this effect is called the *converse piezoelectric effect*. Both effects are described by a set of constitutive equations (IEEE Standard 1989) which are as follows:

$$S_i = s_{ij}^E \sigma_j + d_{mi} E_m \tag{2.1}$$

$$D_m = d_{mi} \sigma_i + \epsilon_{mk}^T E_k \tag{2.2}$$

where S stands for the mechanical strain, σ for the mechanical stress, D for the electrical displacement and E for the electric field. The elastic, piezoelectric and dielectric constants are represented by s^E, d and ϵ^T. The subscriptions $i, j = 1, 2..6$ account for the cartesian direction of the input and the reaction respectively. Equation (2.1) is related to the converse effect and (2.2) to the direct piezoelectric effect. Regarding the strain sensor, the direct piezoelectric effect is utilized to interpret the tube's deflection as a certain voltage. For this purpose the electrode opposite to the actuated one is devoted and evaluated for displacement determination.

2.5 Grounding

Adequate grounding is an important issue for precise and correct measurement. It is even more important when it comes to measurements of small voltage range signals as the relative error becomes proportionally larger. The laboratory is set up to reduce the noise influence to a minimum but also to minimize any cross influences between different actuators, sensors and amplifiers. For this reason the capacitance measurement was, via an isolating transformer, completely decoupled from the main power supply. This impedes grounding loops which can elevate the ground level and distort the measuring signal. In detail the capacitance measurement circuit is set up as shown in Figure 2.4.

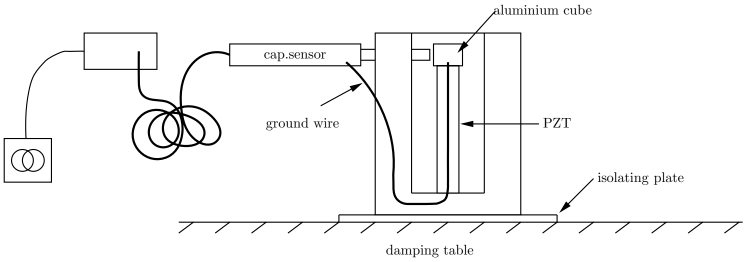

Figure 2.4: Grounding schematics of the capacitive sensor

The probe is mounted and fixed in the outer casing of the setup. The aluminium cube on the top of the tube is directly connected to the casing but isolated from the system. With this the shortest and best way of grounding is realized. In addition an isolating plate between the casing and the vibration table avoids the aforementioned ground loop between the capacitance measurement and the PZT circuit. The inner electrode of the piezoelectric tube is connected to the vibration table which is on ground level. Furthermore the data acquisition card (dSpace) is on the same ground level as the table and the tube. A total setup can be assumed as followed:

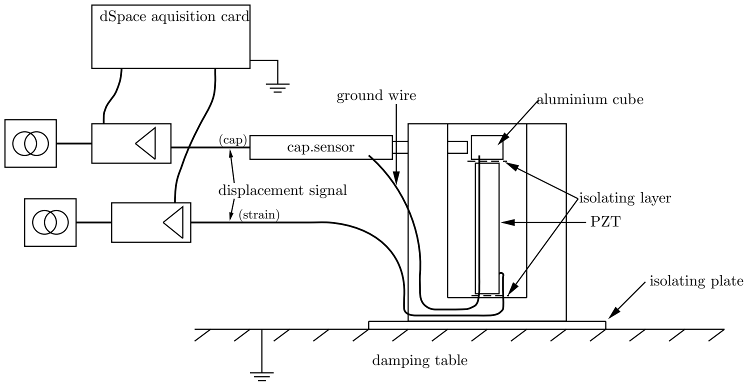

Figure 2.5: Grounding schematics of the lab setup

Chapter 3

System modelling

> Happiness is only real when shared.
>
> Christopher McCandless

Piezoelectric actuators are able to reach resolutions down to 1pm. To control and measure such small displacements, sufficient knowledge of the PZT-system is an essential matter. In this section different parts of a PZT setup are discussed. The most convenient way for estimation and control purposes is a dynamical model given in state space form in order to alleviate the upcoming tasks in Chapter 5.

3.1 System overview

The sensor and amplifier dynamics turn out to be simple high-/low pass filter systems. These can be described straight forward as LTI-models and added to the overall model. Disproportionately more difficult is the description of the piezotube itself. An electromechanical model based on a principal physical relation is established in Chapter 4. This contains a first order differential equation, which describes the hysteresis effects and a differential equation accounting for the mechanical behaviour. These parts are discussed later on in this chapter. During the thesis the traditional possibility of voltage steering was chosen. For this reason the upcoming discussions concentrate more on voltage steering and discuss its included problems rather than those for charge steering.

3.2 Mechanical model

The focus of this section are the mechanical relations of a piezoelectric tube. The intention is to obtain a simple dynamic model for lateral motion, which can be used for further applications. More elaborate models can be found in [21], whereas [25] was used as a reference in the following. PZT constants and properties used throughout the thesis can be found in Table 3.1.

Property	Symbol	Value
Tube length	L	63.5 mm
Inner Radius	R_i	4.76 mm
Outer Radius	R_o	4.48 mm
Average Radius	$\bar{r}$	4.59 mm
Cross Section Area	A	458.3 mm^2
Density	ρ	7500 kg/m^3
Cube mass	m	2.84 g
Piezoelectric Strain Constant	d_{31}	-265 pm/V
Relative Permittivity Constant	ϵ_{33}	3400

Table 3.1: PZT constants.

Longitudinal dynamics are not taken into consideration although the modelling and thus the dynamic behaviour is very similar to the lateral dynamics. The piezoelectric tube actuator is assumed to be a simple forced beam with an attached mass at the end.

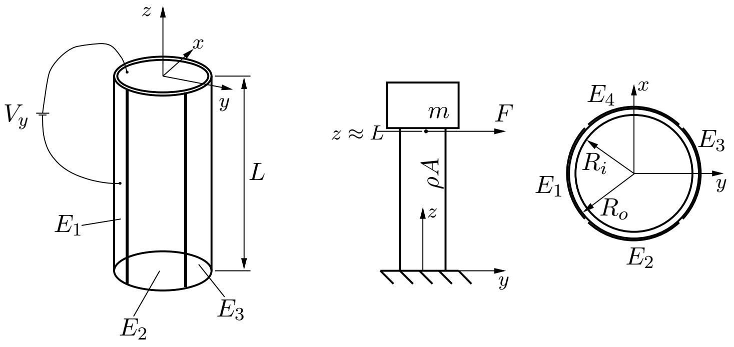

Figure 3.1: Illustration of a piezoelectric tube actuator.

An appropriate illustration is given in Figure 3.1. The PZT is deflected in y-direction by applying a voltage V_y to one of the electrodes E_1 or E_3. According to [26], [25] rotational effects of the beam are negligible and the lateral dynamics can be described as:

$$\rho A\frac{\partial^2\omega}{\partial t^2}+C_\omega\frac{\partial\omega}{\partial t}=-\frac{\pi\bar{r}^3\left(R_o-R_i\right)}{s_{11}^E}\frac{\partial^4\omega}{\partial z^4} \tag{3.1}$$

C_ω is a damping coefficient, $\omega=\omega(z,t)$ describes the deflection in y-direction and A is the cross sectional area of the PZT. Remaining coefficients are described in Figure 3.1 and Table 3.1. The boundary conditions for (3.1) are:

$$\omega=0\,|_{z=0} \tag{3.2}$$

$$\left.\frac{\partial\omega}{\partial z}=0\,\right|_{z=0} \tag{3.3}$$

$$\left.M\frac{\partial^2\omega}{\partial t^2}+C_\omega\frac{\partial\omega}{\partial t}+\frac{\pi\bar{r}^3\left(R_o-R_i\right)}{s_{11}^E}\frac{\partial^3\omega}{\partial z^3}=0\,\right|_{z=L} \tag{3.4}$$

$$\left.\frac{\pi\bar{r}^3\left(R_o-R_i\right)}{s_{11}^E}\frac{\partial^2\omega}{\partial z^2}+\frac{2\sqrt{2}\bar{r}^2d_{31}V_z}{s_{11}^E}=0\,\right|_{z=L} \tag{3.5}$$

For analytical convenience a virtual slice between the mass and the PZT is inserted. This will change (3.1) and boundary condition (3.5) to:

$$\rho A\frac{\partial^2\omega}{\partial t^2}+C_\omega\frac{\partial\omega}{\partial t}+\frac{\pi\bar{r}^3\left(R_o-R_i\right)}{s_{11}^E}\frac{\partial^4\omega}{\partial z^4}=\frac{\partial}{\partial z}F \tag{3.6}$$

$$\left.\frac{\pi\bar{r}^3\left(R_o-R_i\right)}{s_{11}^E}\frac{\partial^2\omega}{\partial z^2}=0\,\right|_{z=L} \tag{3.7}$$

With the method of separation of variables [10] $\omega(z,t)=W(z)T(t)$ where $W(z)$ is achieved by boundary conditions 1 and 2:

$$W_n(z)=C_n\left\{\left(\cos k_nz-\cosh k_nz\right)+\alpha_n\left(\sinh k_nz-\sin k_nz\right)\right\} \tag{3.8}$$

The n^{th} natural frequency ω_n can be found by the characteristic equation:

$$k_nL\left(\cos k_nL\cosh k_nL+1\right)+\frac{m}{\rho AL}\left(\cos k_nL\sinh k_nL-\cosh k_nL\sin k_nL\right)=0 \tag{3.9}$$

The mechanical model can therefore be extended to an appropriate n^{th} order model, which appears to be:

$$M_n\ddot{T}(t)+C_n\dot{T}(t)+K_nT(t)=Q_n \tag{3.10}$$

Coefficients M_n,C_n,K_n and Q_n are the mass, damping, stiffness and force coefficients respectively. These coefficients are calculated as:

$$M_n = \rho A \left(\frac{L}{2} - \frac{a}{4\omega_n} \sin\left(\frac{2\omega_n L}{a} \right) \right) + m \sin^2 \left(\frac{\omega_n L}{a} \right) \tag{3.11}$$

$$C_n = C\rho A \left(\frac{L}{2} - \frac{a}{4\omega_n} \sin\left(\frac{2\omega_n L}{a} \right) \right) \tag{3.12}$$

$$K_n = \omega^2 M_n \tag{3.13}$$

$$Q_n = F_v \left(W_n(L) - \frac{\partial W_n(L)}{\partial z} \right) \Bigg|_{F_v = \frac{2\sqrt{2}\bar{r}^2 d_{31} V_y}{s_{11}^E}} \tag{3.14}$$

An equivalent second order model can be approximated as:

$$\frac{x(s)}{V_y(s)} = \frac{b_u}{s^2 + a_1 s + a_0} \tag{3.15}$$

For further insight and a more exact derivation a detailed explanation is given in [26]. For modelling reasons a transfer function between $\frac{x(s)}{q(s)}$ is most suitable, as no hysteresis effects can be expected when the charge is considered as the input signal. To achieve this, (3.15) is reformulated and leads to the transfer function:

$$\frac{x(s)}{q(s)} = \frac{b_0}{s^2 + a_1 s + a_0} \tag{3.16}$$

When it comes to the accumulation of an equivalent state space model, care is taken on the particular state variables and their physical relevance. This means both the displacement and its first derivative (velocity) are explicitly given as state variables. As a result of that consideration, a state space model is given as:

$$\begin{aligned} \dot{\begin{bmatrix} x_1 \\ x_2 \end{bmatrix}} &= \begin{bmatrix} 0 & 1 \\ -a_0 & -a_1 \end{bmatrix} \begin{bmatrix} x_1 \\ x_2 \end{bmatrix} + \begin{bmatrix} 0 \\ b_0 \end{bmatrix} q \\ y &= \begin{bmatrix} 1 & 0 \end{bmatrix} \begin{bmatrix} x_1 \\ x_2 \end{bmatrix} \end{aligned} \tag{3.17}$$

a_0	3.454×10^7
a_1	15.12
b_0	1.922×10^8
b_u	3.0188

Table 3.2: Related constants, mechanical model.

3.2.1 Model comparison

A mathematical model based on physical relations is always a good way to investigate the general behaviour. Unfortunately the exact values (resonance frequency, attenuation, amplification) rarely match the real system. A reason for this could be un-modelled phenomena, uncertain material parameters or model simplifications. To adapt the dynamics to the real model one can accomplish a spectral analysis. To compare the $\frac{x(s)}{q(s)}$ transfer functions, a displacement and charge measurement are necessary. The tube deflection $x(s)$ is derived from the capacitive sensor whereas the charge $q(s)$ can be gained via a voltage drop measurement over a capacitor. A comparable circuitry is given in Figure 3.2.

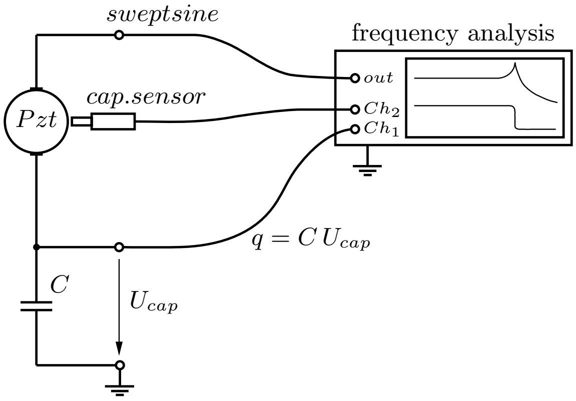

Figure 3.2: Circuitry of a frequency analysis for the mechanical model

Figure 3.3 compares both frequency responses. An excellent compliance between the physical model and the measured equivalent can be detected. This supports the physical based calculations and verify the validity of the model. Observing the first resonance peak ($\approx 928\,Hz$) of the two curves one can register an insignificant difference of $\Delta f \approx 0.4\,Hz$.

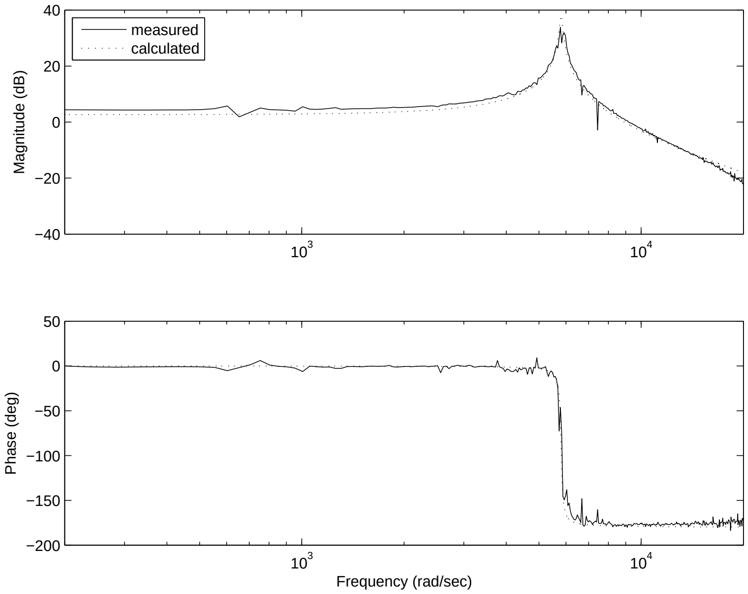

Figure 3.3: Measured and calculated frequency response

3.3 Hysteresis model

In the past, the piezoeletric tube actuators have been widely used is several positioning applications. Consistent with that, the demand for more accuracy by means of displacement is followed by more accurate system models. Nonlinear hysteresis effects constrain the positioning precision significantly. In order to achieve sufficient accurate motion within nanometer manipulation, special care has to be taken on developing appropriate models for such hysteresis effects. Several different models have been developed over the course of time as hysteresis behaviour can be observed in many different fields (e.g. in friction, plasticity, ferromagnetism and also piezoelectricity). Mathematically speaking, the hysteresis effect can be described as a dynamical system with one input and an output variable invariant with respect to time scale changes. Often such a system is called a rate independent (or persistent) dynamical system. In the following some common models are considered with respect to complexity, accuracy and usability for control design purposes.

A general hysteresis nonlinearity could be described as:

$$\begin{aligned} w(t) &= F(v(t)) \\ &= \begin{cases} a(v(t)-b), & \text{if}\, \dot{v}(t) > 0 \,\text{and}\, a(v(t)-b) \\ a(v(t)+b), & \text{if}\, \dot{v}(t) < 0 \,\text{and}\, a(v(t)+b) \\ w(t-), & \text{else} \end{cases} \end{aligned} \tag{3.18}$$

The parameter a describes a linear slope whereas the constant b is the backlash distance. This model is obviously discontinuous and cannot be used for any system modelling purposes or control design issues.

3.3.1 Dahl model

At first the Dahl hysteresis model was developed to describe friction nonlinearities. In [12],[6] the Dahl model is given as:

$$\frac{dF}{dx} = \sigma \left(1 - \frac{F}{F_c}\, sgn(v)\right)^{\alpha} \tag{3.19}$$

The coefficient σ appears to be the stiffness parameter whereas α mainly determines the shape of the curve. For most applications $\alpha = 1$ is used. The force F will never exceed F_c as long as the initial value satisfies $|F(0)| < F_c$. With the displacement and the sign of the velocity as the only inputs, the model is *rate independent*[*] which (as named earlier) is an important property of the model. Time dependency of the model can be obtained as:

$$\frac{dF}{dt} = \frac{dF}{dx}\frac{dx}{dt} = \frac{dF}{dx} v = \sigma \left(1 - \frac{F}{F_c} sgn(v)\right)^{\alpha} v \tag{3.20}$$

The fact that a force-displacement relation is described, motivates the idea of modelling a hysteresis loop between a voltage and charge with the same model. In [17] an appropriate second order model based on Dahl's observations is introduced. It is described by:

$$\frac{dF^2}{dt^2} + sgn\,(v)\, a_1 \frac{dF}{dt} + a_2 F = sgn\,(v)\, b_1 \frac{dU}{dt} + b_0 U \tag{3.21}$$

---

[*] A rescaling of the input with respect to time does not instantly lead to a rescaling of the output.

With the domains changed to voltage and charge respectively, a corresponding state space implementation is of the form:

$$\dot{\begin{bmatrix} x_1 \\ x_2 \end{bmatrix}} = \begin{bmatrix} 0 & 1 \\ -a2 & -sgn\left(\dot{v}\right) a_1 \end{bmatrix} \begin{bmatrix} x_1 \\ x_2 \end{bmatrix} \frac{dU}{dt} + \begin{bmatrix} 0 \\ 1 \end{bmatrix} \frac{dU}{dt} \tag{3.22}$$

$$q = \begin{bmatrix} b_1 & sgn\left(\dot{v}\right) b_0 \end{bmatrix} \begin{bmatrix} x_1 \\ x_2 \end{bmatrix} \tag{3.23}$$

a_2	4.41×10^{-4}
a_1	1
b_0	7.8×10^{-6}
b_1	1.76×10^{-9}

Table 3.3: Related constants, Dahl model

Simulations with voltage as input and the charge as the output of the system obtain hysteresis characteristics as Figure 3.5 illustrates. Basically the modelling results are quite satisfying but simulations show a wrong loop direction. Hence this model is inappropriate for piezo hysteresis implementations but another model presented in Section 3.3.2 is used for further calculations instead.

3.3.2 Coleman-Hodgdon model

3.3.2.1 Explanation

Derivation and constraints Unlike the inclusion of discontinuities as in (3.18), Coleman and Hodgdon introduced a *continuous time model* describing the hysteresis effect. Originally designed for ferromagnetism the model upon a class of constitutive relations is defined as:

$$\dot{B} = \alpha|\dot{H}|\left[f\left(H\right) - B\right] + \dot{H} g\left(H\right) \tag{3.24}$$

where the parameter H is the magnetic field and B the flux. This solution can be adapted to a piezoelectric hysteresis problem simply by rewriting (3.24) to:

$$\frac{dw(t)}{dt} = h\left(v(t), \dot{v}(t), w(t)\right) \tag{3.25}$$

where

$$h\left(v(t),\dot{v}(t),w(t)\right)=f\left(v(t),w(t)\right)\left|\dot{v}(t)\right|+g\left(v(t),w(t)\right)\dot{v}(t) \tag{3.26}$$

With respect to control purposes, [19] suggested to just allow differential models with a function $f(v(t),w(t))$ affine in $w(t)$ and for the function $g(v(t),w(t))$ being a constant in $w(t)$. With these assumptions the differential hysteresis model shows the form:

$$\dot{w}=\alpha\left|\dot{v}\right|\left(f(v)-w\right)+\dot{v}g(v) \tag{3.27}$$

where the constant α is only allowed to be $\alpha>0$. In [18] the above dynamical model (3.27) has been used to simulate and describe the ferroelectric hysteresis. For that purpose following constraints concerning the functions $f(\cdot)$ and $g(\cdot)$ were set up.

1. $f(\cdot)$ is real and odd. Furthermore it has to be monotonously increasing and continuously differentiable.

2. $g(\cdot)$ is real, even, piecewise continuous and has to have a finite value at infinity such that:

$$\lim_{s\to+\infty}\frac{df(s)}{ds}=\lim_{s\to+\infty}g(s) \tag{3.28}$$

3. Functions $f(\cdot)$ and $g(\cdot)$ are such that :

$$g(s)\leq\frac{df(s)}{ds}\qquad\vee\, s<\infty \tag{3.29}$$

In [1] position measurements have been performed showing the hysteresis loop between a low frequency voltage input signal and the corresponding output. The simulated loop is similar to the ferromagnetic hysteresis loop shape discussed in [9]. Based on those simulations, the following choice for the functions $f(\cdot)$ and $g(\cdot)$ are proposed.

$$f(v)=\begin{cases}av_{max} & \text{if}\quad v_{max}<v,\\ av & \text{if}\quad -v_{max}\leq v\leq v_{max},\\ av_{min} & \text{if}\quad v<-v_{max}\end{cases}$$

and

$$g(v) = \begin{cases} 0 & \text{if} \quad v_{max} < v, \\ b & \text{if} \quad -v_{max} \le v \le v_{max}, \\ 0 & \text{if} \quad v < -v_{max} \end{cases}$$

With $a > 0$ and $b > 0$ clearly the functions $f(\cdot)$ and $g(\cdot)$ meet the conditions of 1 and 2. The inequality of (3.29) is also fulfilled such that $\frac{1}{2}\, a \le b \le a$. Function $f(\cdot)$ is proportional to its input v whereas the function $g(\cdot)$ is constant with respect to v. This leads to the final differential equation adequate for piezoelectric purposes:

$$\dot{w} = \alpha\, |\dot{v}|\, (av - w) + b\, \dot{v} \tag{3.30}$$

or expressed with charge q and voltage u:

$$\dot{q} = \alpha\, |\dot{u}|\, (au - q) + b\, \dot{u} \tag{3.31}$$

Switching mechanism In order to test the switching ability of the model some pre-definitions are required. According to [30] an explicit solution to (3.30) can be found as follows:

$$w(t) = av(t) + d(v) \tag{3.32}$$

where v is piecewise monotonous. For the term $d(v)$ one can state:

$$d(v) = [w_o - av_o]\, e^{-\alpha(v-v_o)sgn(\dot{v})} + e^{-\alpha v sgn(\dot{v})} \int_{v_o}^{v} [b - a]\, e^{\alpha\psi sgn(\dot{v})} d\psi \tag{3.33}$$

with $\dot{v}$ being constant and $w(v_o) = w_o$. Assuming the initial values (v_o, w_o) boundaries for the term $d(v)$ can be found:

$$\lim_{v\to\infty} d(v) = -\frac{a-b}{\alpha} \tag{3.34}$$

$$\lim_{v\to-\infty} d(v) = \frac{a-b}{\alpha} \tag{3.35}$$

For $\dot{v} > 0$ the initial values $w_o = 0$ and $v_o = 0$ are introduced. Inserting them in (3.32) and (3.33), $w(t)$ is given as:

$$w(t) = av(t) - \frac{a-b}{\alpha}\left(1 - e^{-\alpha v(t)}\right) \quad \text{for } \dot{v} > 0 \tag{3.36}$$

Under the initial assumptions given above, $v(t)$ is constantly increased until a time t_r where v_r is reached. For $t > t_r$ $v(t)$ is decreased again ($v(t) < v_r$). With remark to $\dot{v} < 0$ the function for $w(t)$ is given by:

$$w(t) = av(t) + \frac{a-b}{\alpha}\left[1 - \left(2e^{-\alpha v_r} - e^{-2\alpha v_r}\right) e^{\alpha v(t)}\right] \quad \text{for } \dot{v} < 0 \tag{3.37}$$

Analysis of (3.36) and (3.37) shows $w(t)$ switching from $av(t) - \frac{a-b}{\alpha}$ to $av(t) + \frac{a-b}{\alpha}$ generating a hysteresis like curvature.

3.3.2.2 Parameterisation

The characteristics of the aforementioned hysteresis loop can be determined experimentally. Via approximated formulae derived in [19] the 3 parameters a, b, α can be determined using the approximations:

$$\delta \approx \alpha\left(\frac{a}{b} - 1\right) A^2 \tag{3.38}$$

$$\eta \approx \alpha\,(a-b)\,A^2 \tag{3.39}$$

$$\epsilon \approx \frac{4}{3}\alpha\,(a-b)\,A^3 \tag{3.40}$$

The parameters δ, η and ϵ are calculated via taking some characteristic hysteresis points into charge. Those appear as shown in Figure 3.4 and are calculated as:

$$\delta \triangleq v_{\uparrow} - v_{\downarrow} \tag{3.41}$$

$$\eta \triangleq w_{\downarrow} - w_{\uparrow} \tag{3.42}$$

In addition to that, the area encircled by the loop is given as ϵ. With those parameters being determined and the knowledge of the input signal characteristics one can calculate the corresponding parameters describing such a hysteresis loop model. In Figure 3.5 the

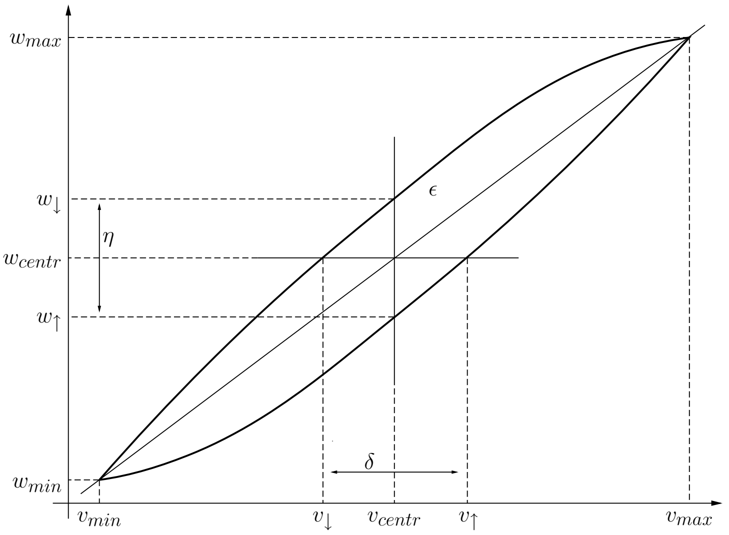

Figure 3.4: Parameters of a hysteresis loop

resulting hysteresis is compared with the simulation results of the foregone Dahl model. Table 3.4 gives the computed values for the corresponding loop.

3.3.2.3 RLS-parameterisation

General background In Section 3.3.2.2 a rough, intuitive method for hysteresis parameterisation was presented. In this Section the advantages of adaptive algorithms are utilized to determine the hysteresis parameters. As an alternative to the Wiener-filter theory, a recursive least square (RLS) based algorithm was implemented for this purpose of adaption. Different to other filters, the RLS algorithm is not related to any statistics of the signals, but directly calculates the data with the information available up to the current point. The deterministic cost function is defined as the sum of the squared error values from time l_0 to k:

$$J_k = \sum_{l=l_0}^{k} |e[l]|^2 = \sum_{l=l_0}^{k} |y[l] - d[l]|^2 \tag{3.43}$$

The output of the algorithm is a weighting factor which minimizes J_k and is optimal with respect to the data available up to point k. To be able to calculate the optimal weighting vector $\underline{w}_k$, the cost function J_k has to be minimized. Therefore the gradient of J_k (with respect to $\underline{w}_k$) is calculated and set equal to $\underline{0}$ (Compare (3.45)). After replacing

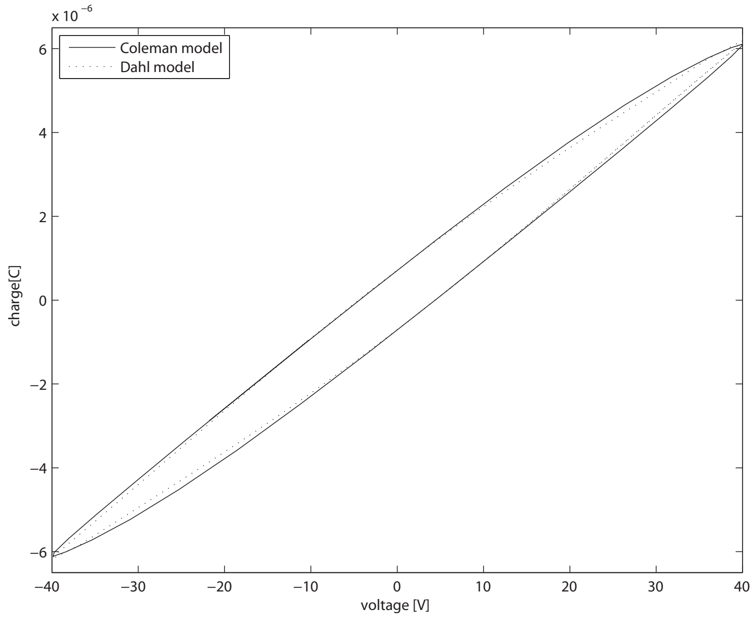

Figure 3.5: Hysteresis loop simulated by the Dahl and Coleman model. The charge is displayed as a function of the input voltage

several vector products by its correlation matrices, the deterministic cost function J_k can be rewritten as:

$$J_k = \underline{w}_k^T \mathcal{R}_k \underline{w}_k - 2\underline{w}_k^T \underline{\mathcal{P}}_k + \sum_{l=l_0}^{k} d^2[l] \tag{3.44}$$

The gradient then appears to be:

$$\nabla \underline{w} \{J_k\} = (2\mathcal{R}_k \underline{w}_k - 2\underline{\mathcal{P}}_k) = \underline{0} \tag{3.45}$$

This yields the optimal weighting factor $\underline{w}_k$:

$$\underline{w}_k = \mathcal{R}_k^{-1} \underline{\mathcal{P}}_k \tag{3.46}$$

With this, a set of iterative equations could be given but unfortunately at a rather high calculation complexity. With matrix simplification rules, as described in [23] a more effective way is introduced. Those simplifications then lead to the following iteration steps for the RLS algorithm:

- Initialisation:

$$\hat{\mathcal{R}}_0^{-1} = \eta \mathbf{I}_N \tag{3.47}$$

$$\underline{w}_0 = \underline{0} \tag{3.48}$$

- Iterative steps at time $k = 1, 2, 3, ...$:

  1. A priori output value:

  $$y[k] = \underline{x}^T[k]\underline{w}_{k-1} \tag{3.49}$$

  The a priori output value is calculated with help of the current vector $x[k]$ and the last optimal weighting factor $\underline{w}_{k-1}$. As there is no updated $\underline{w}_k$ available yet, hence it is called a priori value.

  2. A priori error:

  $$e[k] = d[k] - y[k] \tag{3.50}$$

  The difference between the desired value $d[k]$, which is available from the unknown system and the a-priori output value $y[k]$ results in the a-priori error.

  3. Filtered, normalised data vector:

  $$\underline{\tilde{z}}_k = \frac{\mathcal{R}_{k-1}^{-1}\underline{x}[k]}{\rho + \underline{x}^T[k]\mathcal{R}_{k-1}^{-1}\underline{x}[k]} \tag{3.51}$$

  The data vector $\underline{\tilde{z}}_k$ can be interpreted as a filtered value of $\underline{x}[k]$. The autocorrelation matrix R_{k-1}^{-1} has influence in both length and direction. Additional to that the factor ρ is added in the denominator. With this factor being 1 the initial matrix would still have influence on the weighting factor. Chosen somewhere between $0.95 - 1$ this influence vanishes by the run of time. ρ is therefore also called *forgetting factor* as it forgets about the initialised values. A value of memory can be described by $g(\rho)$:

  $$g(\rho) = \frac{1}{1-\rho} \quad \text{with} \quad 0 < \rho \leq 1$$

4. Update of the optimal weighting factor:

$$\underline{w}_k = \underline{w}_{k-1} + e[k]\underline{\tilde{z}}_k \tag{3.52}$$

Updating the weighting factor is based on the old weighting factor $\underline{w}_{k-1}$, where only the correction term $e[k]\underline{\tilde{z}}_k$ is added. This correction term is finally dependent on the last updated values $\underline{x}[k]$ and $d[k]$. Consider therefore also:

$$e[k] = d[k] - y[k] = d[k] - \underline{x}^T[k]\underline{w}_{k-1}$$

5. Update of the inverse deterministic autocorrelation matrix:

$$\mathcal{R}_k^{-1} = \frac{1}{\rho}\left(\mathcal{R}_{k-1}^{-1} - \underline{\tilde{z}}_k\underline{x}^T[k]\mathcal{R}_{k-1}^{-1}\right) \tag{3.53}$$

Dependent on the old value, the new inverse autocorrelation matrix is calculated with respect to ρ as well as to the filtered and unfiltered data vectors $\underline{\tilde{z}}_k$,$\underline{x}^T[k]$.

RLS algorithm implementation In order to apply the RLS algorithm on the hysteresis problem some predefinitions are necessary. From (3.30) the hysteresis description is given as:

$$\dot{q} = \alpha|\dot{U}|\,(aU - q) + b\dot{U} = \alpha a\underbrace{|\dot{U}|U}_{x_1} - \alpha\underbrace{|\dot{U}|q}_{x_2} + b\underbrace{\dot{U}}_{x_3} \tag{3.54}$$

The RLS algorithm requires an input vector $\underline{x}$, a desired signal d and a weighting vector $\underline{w}$. Evidently $d = \dot{q}$ and derived from (3.54), the input vector $\underline{x}$ and the weighting vector $\underline{w}$ are defined as follows:

$$\underline{x} = \begin{bmatrix}|\dot{U}|U\\|\dot{U}|q\\\dot{U}\end{bmatrix} = \begin{bmatrix}x_1\\x_2\\x_3\end{bmatrix} \qquad \underline{w} = \begin{bmatrix}\alpha a\\-\alpha\\b\end{bmatrix} = \begin{bmatrix}w_1\\w_2\\w_3\end{bmatrix} \tag{3.55}$$

For lab implementations the inputs U and $|\dot{U}|$ are directly derived from the triangle signal source given by a waveform generator. Concerning the measurements of q and $|\dot{q}|$ the problem of derivation has to be kept in mind. Derivating a noisy signal can lead to inadequate results hence it is rather suggested to measure $\dot{q}$ (if possible) and integrate this signal to obtain q. A good possibility to measure $\dot{q}$ is given via a current measurement where $\dot{q} = i$. The usage of a simple current amplifier gives satisfying results and is one alternative to provide $\dot{q}$. A possible circuitry is illustrated in Figure 3.6.

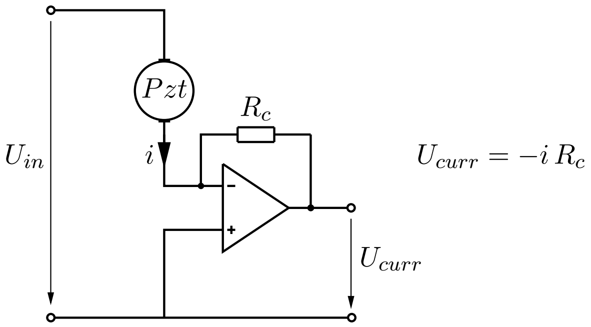

Figure 3.6: Circuit for current measurements

Results from the RLS estimation were compared with some measured data. The outputs presented in Figure 3.7 are not exactly identical but give a good approximation to simulate the effects of hysteresis. A comparison between the found parameters from Section 3.3.2.2 and the parameters from the RLS algorithm is given in Table 3.4 and shows quite considerable discrepancies in the parameters a and α. Only parameter b appears to be roughly equal. Furthermore the RLS algorithm does not meet the requirement

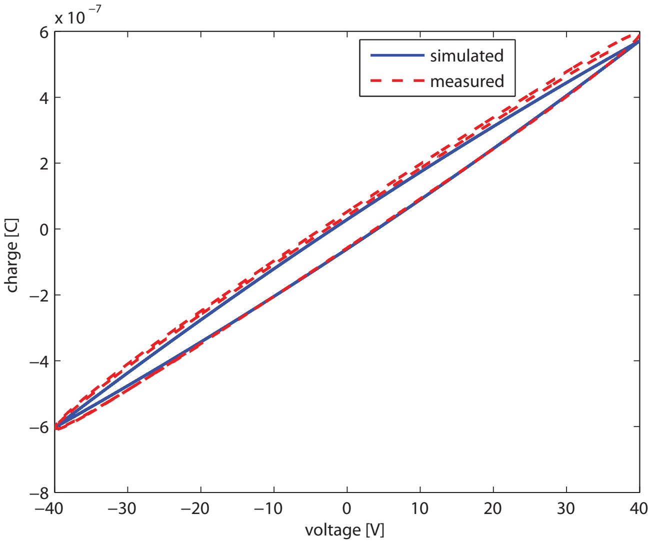

Figure 3.7: Comparison of measured and simulated data

$\frac{1}{2}\,a \leq b \leq a$. Nevertheless, for further investigations the RLS parameters are employed.

	a	b	α
RLS estimation	$6.95\,10^{-6}$	$1.468\,10^{-8}$	$8.045\,10^{-6}$
approximate estimation	$1.625\,10^{-8}$	$1.2\,10^{-8}$	0.055

Table 3.4: Comparison of approximated and RLS estimated parameters

3.4 Creep model

The displacement response of a piezoelectric tube has been modelled and discussed in Section 3.2. The response is determined by the mechanical coherences and is typically only a few milli-seconds. This fast response is followed by a slow creeping response in the range of some seconds to several minutes. According [27] such creep effects can be up to 20% of the total response. In [11] it is found, that an appropriate model to also simulate the creep response can simply be a composition of springs and dampers. An equivalent possible schematic is presented in Figure 3.8. A frequency response has already been introduced in Section 3.2 but with focus rather on the general dynamics and natural frequencies. Omitted at that point was the very small variation in phase and gain at low frequencies ($\sim 20Hz - 300Hz$). From Section 3.2 Figure 3.3 is re-plotted but with a zoomed area around the frequencies of interest. Clearly a gain decrease can be observed with increasing frequency, which affirms the presence of creep effects. According to [27], the *relative degree*[†] δ is 0 for a transfer function $\frac{x(s)}{q(s)}$ at frequencies much lower than the first resonant frequency. Subsequent to that the behaviour in Figure 3.9 seems confirmable and a model as given in Figure 3.8 appears suitable. To eliminate possible hysteresis effects, the applied voltage/load was kept small and the system response was measured over an

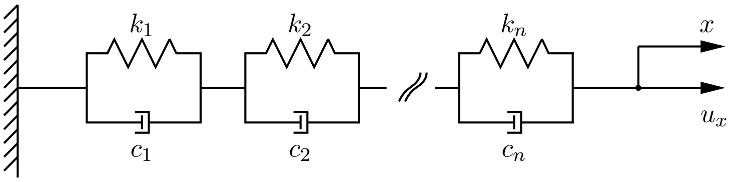

Figure 3.8: Schematic model to simulate creep effects

[†] The relative degree is defined as the difference between the number of poles and number of zeros ($\delta = \sum p - \sum n$)

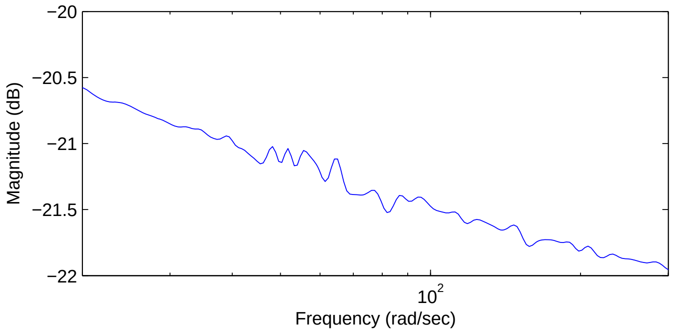

Figure 3.9: Slight decrease in gain with increased frequency

extended period of time. Thus at low magnitudes and extremely low frequencies the creep effect can be isolated from all the other effects. The system response on a step input is given in Figure 3.10. In [11] the model order has been determined by an error comparison

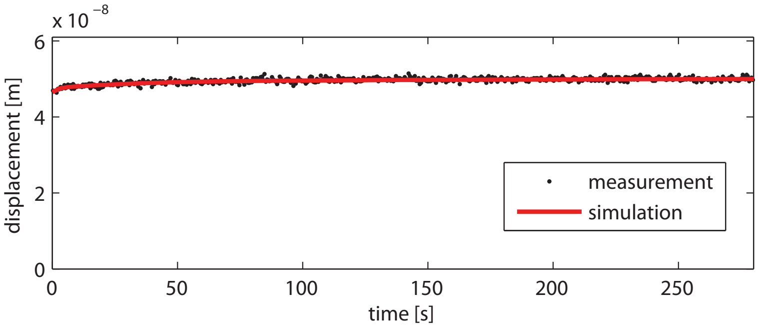

Figure 3.10: Comparison of measured and simulated creep effects

of different order creep models where the standard deviation σ is calculated as:

$$\sigma_c = \sqrt{\frac{1}{N_{cx}-1}\sum_{i=1}^{N_{cx}}(x_i-\bar{x}_i)^2} \tag{3.56}$$

and the maximum error appears to be:

$$E_{max} = \max_i |x_i - \bar{x}_i| \tag{3.57}$$

Within here the model has been assumed as of order 3. The respective characteristic values are given in Table 3.5.

order	σ	E_{max}
3	4.393×10^{-10}	1.198×10^{-9}

Table 3.5: Characteristic creep model values

The creep model is given as:

$$G_{creep} = \frac{s^3\,4.649\times10^{-8} + s^2\,2.457\times10^{-8} + s\,7.938\times10^{-10} + 2.363\times10^{-12}}{s^3 + s^2\,0.516 + s\,0.0161 + 4.69\times10^{-5}} \tag{3.58}$$

and the corresponding time response is displayed in Figure 3.10 where the simulation is compared to the measured response.

3.5 Capacitive sensor model

3.5.1 Model

Preconditions and implementation methods of the capacitive sensor have already been discussed in Section 2.3. For simulation purposes the capacitive sensor should be available as a dynamic model as well. The sensitivity S_c is given in the data sheet of the sensor. The dynamic model was at this point not determined by means of measurements or frequency analysis but rather taken from the supplier. The transfer function is said to be a simple low pass filter with a cut-off frequency at some hundred kHz. Together this gives the following transfer function and state space model respectively.

$$\begin{aligned}
&\frac{U_c(s)}{x_1(s)} = S_c\,\frac{2\pi f_c}{s+2\pi f_c} = \frac{K_c}{s+w_c}\\
&\dot{U}_c = \begin{bmatrix}-w_c\end{bmatrix} U_c + \begin{bmatrix}K_c\end{bmatrix} x_1\\
&y = \begin{bmatrix}1\end{bmatrix} U_c
\end{aligned} \tag{3.59}$$

f_c	$100\,kHz$
w_c	$628.3\times10^3\,1/s$
S_c	$0.2\times10^6\,V/m$
K_c	$1.256\times10^{11}\,V/sm$

Table 3.6: Related constants, capacitive sensor

3.5.2 Zero offset with LMS algorithm

To provide a zero-mean sensor signal to the Kalman filter, the bias error has to be subtracted from the actual signal. The fact that the bias error itself cannot be considered as constant, requires some kind of estimation. Countless methods of estimation are available where the least-mean-square-method (LMS) is one possibility. The basic idea for all kinds of gradient methods (the LMS algorithm is one of them) is to search the minimum of the error surface. For this, the actual weighting factor $\underline{w}[k]$ is manipulated with an adjustment term to calculate the updated vector $\underline{w}[k+1]$. With the adjustment term being the negative gradient of the error surface, the weighting factor approaches the optimal solution with each step. The gradient appears to be:

$$\nabla_{\underline{w}}\left\{J(\underline{w})\right\} = 2\left(\mathbf{R}\underline{w} - \underline{p}\right) \tag{3.60}$$

To calculate the gradient, knowledge about the statistics ($\mathbf{R}$ and p) of the signals is required. As this is often not available, an estimated gradient is used requiring observability of the signals $x[k]$ and $d[k]$ only. The LMS does not provide the optimal solution (due to the estimated gradient usage), but still sufficient results at acceptable convergence times are achieved. The LMS algorithm appears then as follows:

Initialisation:

$$\underline{w}[0] = \underline{0} \qquad \mu > 0: \quad \text{constant step size}$$

At each step $k = 0, 1, 2, ...$:

- Filter output value:

$$y[k] = \underline{w}^T[k]\underline{x}[k] \tag{3.61}$$

- Error value:

$$e[k] = d[k] - y[k] \tag{3.62}$$

- Update coefficient vector:

$$\underline{w}[k+1] = \underline{w}[k] + \mu e[k]\underline{x}[k] \tag{3.63}$$

Results of this implementation are plotted in Figure 3.16 where the LMS algorithm is applied on the strain sensor. Principally the same results apply for the discussed capacitve sensor as well.

3.6 PZT strain model

Discussed in the previous Section 3.5 a precise and easy method for measuring displacements has been introduced. The drawback of such a gauging is the rather high equipment costs. A more cost effective possibility of displacement measurement is therefore presented in this Section. The piezotube itself can be used not just as an actuator, as described in Section 3.2 but also as a sensor appointed as what is known as a self sensing actuator. This means actuation can be measured by means of the piezotube itself. Basis to that is the *piezoelectric effect*[‡]. As soon as the PZT is deflected a charge will be generated due to mechanical stress. Related to that, this charge is generated depending on the deflection of the tube. With simple measuring methods, as explained in Section 3.6.2 the charge can be evaluated and interpreted as the tube's deflection.

3.6.1 Sensitivity

The relationship between the occurring deflection and charge is given via a sensitivity constant. A physically based determination of this constant S_s is given in the following. Bending motion of the PZT is measured from a neutral line in z-direction. In Figure 3.11 this is pointed out more clearly. Under the pre-condition of a small field, the constitutive

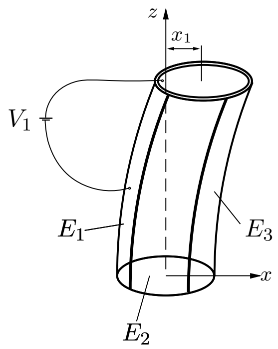

Figure 3.11: PZT bending motion

[‡] compare: the converse piezoelectric effect has been utilized for PZT actuation

relations (already mentioned in (2.2) and (2.2)) for a piezoelectric material in general are given as (IEEE Standard 1987):

$$\begin{bmatrix} S_z \\ D_r \end{bmatrix} = \begin{bmatrix} s_{11}^E & d_{31} \\ d_{31} & \epsilon_3^\sigma \end{bmatrix} \begin{bmatrix} \sigma_z \\ E_r \end{bmatrix} \tag{3.64}$$

where once again S is the strain, D the electric displacement, σ the stress and E the electric field. The strain appearing in the PZT (Compare Figure 3.11) is, according to [10] given as:

$$S_z = -\frac{x_1}{R} = -\frac{\bar{r}\sin\theta}{R} = -\bar{r}\sin\theta\frac{\partial^2 w}{\partial z^2} \tag{3.65}$$

Observe that $\bar{r}$ is the average radius of the PZT whereas R must not be mixed up with the radius of the PZT but rather describes the radius of a curvature (at some point). x_1 describes the lateral deflection. From relations given in (3.64) E_r can be written as:

$$E_r = \frac{D_r s_{11}^E - d_{31} S_z}{\epsilon_r^\sigma s_{11}^E - d_{31}^2} \tag{3.66}$$

Assuming that one applies a voltage V_1 at electrode E_1, relations from above yield to:

$$\begin{aligned} V_1 &= E_r\left(R_o - R_i\right) \\ &= \left(R_o - R_i\right)\frac{D_r s_{11}^E - d_{31} S_z}{\epsilon_r^\sigma s_{11}^E - d_{31}^2} \\ &= -\frac{d_{31}\left(R_o - R_i\right)}{\epsilon_r^\sigma s_{11}^E - d_{31}^2}\frac{\bar{r}\sin\theta}{R} + \frac{s_{11}^E\left(R_o - R_i\right)}{\epsilon_r^\sigma s_{11}^E - d_{31}^2} D_r \end{aligned} \tag{3.67}$$

Upon that, the charge created at electrode E_1 can be considered as:

$$\begin{aligned} Q &= \int_0^L \int_{\theta_1}^{\theta_2} \bar{r} D_r d\theta dz \\ &= \frac{s_1 1^E \epsilon_3^\sigma - d_{31}^2}{s_{11}^E\left(R_o - R_i\right)}\bar{r}\left(\theta_2 - \theta_1\right) L V_z + \frac{d_{31}}{s_{11}^E}\bar{r}^2\left(\cos\theta_2 - \cos_1\right)\left.\frac{\partial w}{\partial z}\right|_{z=L} \end{aligned} \tag{3.68}$$

To solve the aforementioned equation the relationship $\frac{1}{R} = \frac{\partial^2}{\partial z^2}$ and $\left.\frac{\partial w}{\partial z}\right|_{z=0}$ were assumed. Easy to see, neither the voltage nor the charge are functions of the tube deflection in this equation. But instead the angle at the edge of the tube $\left.\frac{\partial w}{\partial z}\right|_{z=L}$ defines the charge. Under the assumption that only the first resonance peak is dominant (this has already been assumed in Section 3.2) one can approximate

$$w|_{z=L} \approx \frac{1}{K_{pr}} \frac{\partial w}{\partial z}\bigg|_{z=L} \tag{3.69}$$

Factor K_{pr} in turn can be determined via (3.8). Indirect proportionality between these two domains result in $\frac{1}{K_{pr}} \approx \frac{W_1}{\frac{dW_1}{dz}}\bigg|_{z=L}$. Inserting this into (3.68) defines the charge as a function of the deflection.

$$\frac{q_{pzt}}{w}\bigg|_{z=L} \approx \frac{d_{31}}{s_{11}^E}\bar{r}^2\left(\cos\theta_2 - \cos\theta_1\right)K_{pr} + \frac{s_11^E\epsilon_3^\sigma - d_{31}^2}{s_{11}^E\left(R_o - R_i\right)}\bar{r}\left(\theta_2 - \theta_1\right)LV_1 \tag{3.70}$$

Under the condition that $V_1 = 0$ the relation reduces to:

$$\frac{q_{pzt}}{w}\bigg|_{z=L} \approx \frac{d_{31}}{s_{11}^E}\bar{r}^2\left(\cos\theta_2 - \cos\theta_1\right)K_{pr} \tag{3.71}$$

Observe that the above relationship is only valid for points at the edge of the tube. By inserting for the constant values the strain sensitivity constant is

$$S_s = \frac{q_{pzt}}{w}\bigg|_{z=L} = 0.0042[C/m] \tag{3.72}$$

3.6.2 Measurement units

3.6.2.1 Voltage amplifier

In general, sensors having a charge output can be connected to voltage amplifiers on conditions that the input resistance of the amplifier is very high. A keen disadvantage of such an arrangement is the impact of several factors on the output voltage. Besides the amplifier input-resistance and capacity, the PZT capacity and cable capacities determine the output signal. (Compare Section 3.6.2.2 where this dependency is not given). Such a structure is given in Figure 3.12 where a dominant high pass behaviour seems obvious. In a first approximation only the PZT capacity and the input resistance were taken into account. For the transfer function and the state space model respectively one can state:

$$\begin{aligned} \frac{U_s(s)}{x_1(s)} &= \frac{S_s}{C_k}\frac{2\pi R_{in}C_{pzt}s}{s + 2\pi R_{in}C_{pzt}} = \frac{K_s s}{s + w_s} \\ \dot{U}_s &= \begin{bmatrix} -w_s \end{bmatrix} U_s + \begin{bmatrix} K_s \end{bmatrix} \dot{x}_1 \\ y &= \begin{bmatrix} 1 \end{bmatrix} U_s \end{aligned} \tag{3.73}$$

The input signal given within the above transfer function is the displacement x_1. Different to that, the corresponding state space model has the displacement derivation $\dot{x}_1$ as its input and is strongly worded an ordinary differential equation only. In order to develop an overall system model, the mechanical tube model explicitely identifies the displacement and the derivation as separate states.

R_{in}	$100\,M\Omega$
C_{pzt}	$13\,nF$
f_{cut}	$0.122\,Hz$
w_s	$0.769\,1/s$
C_k	$3.43 \times 10{-}7$
S_s	$0.0042\,C/m$
K_s	2.7×10^5

Table 3.7: Related constants, voltage amplifier

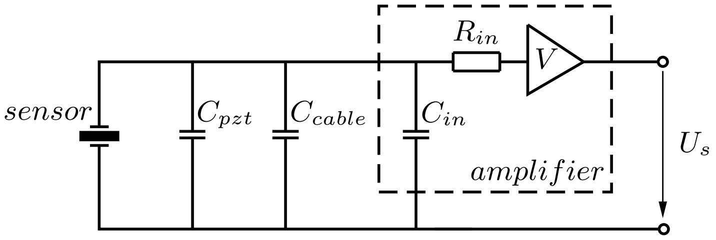

Figure 3.12: Voltage amplifier at the strain output

3.6.2.2 Charge amplifier

A simple and low cost method to convert a charge into a voltage signal is an operational amplifier (op-amp) circuitry. In its simplest form only one op-amp is needed. A possible circuit is illustrated in Figure 3.13.

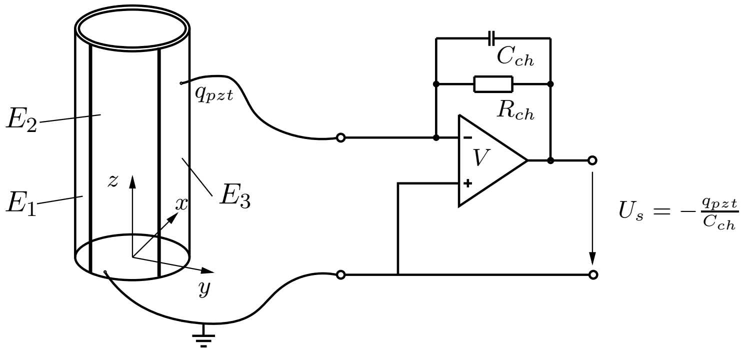

Figure 3.13: Charge amplifier at the strain output

One benefit of this amplifier compared to the one in Section 3.6.2.1 is the independence of the PZT capacity. A drawback is the high DC-gain which amplifies any bias currents and most likely leads to an over steering of the op-amp. To avoid this, a resistor R_{ch} makes sure that a stable 'zero point' voltage at the output is given. The time constant $\tau = R_{ch}\, C_{ch}$ determines the lower cut-off frequency which is $f_{cut} = \frac{1}{2\pi R_{ch} Cch}$. At this point it should be mentioned that the charge amplifier in the given form is not appropriate for measuring static charges. By the run of time, the output voltage decreases at a constant charge input in compliance with the function $U_s = -\frac{q_0}{C_{ch}} e^{\overline{\frac{-t}{R_{ch} C_{ch}}}}$. The amplification factor at $t = 0$ is determined by the feedback capacitor C_{ch} and the adjacent charge $-\frac{q_{pzt}}{C_{ch}}$. A corresponding transfer function can be given as:

$$\frac{U_s}{q_{pzt}} = -\frac{1}{C_{ch}} \frac{w_{ch} s}{s + w_{ch}} \tag{3.74}$$

In combination with the strain sensitivity evaluated in (3.72) the transfer function for the strain sensor is:

$$\frac{U_s(s)}{x_1(s)} = -S_s \frac{1}{C_{ch}} \frac{w_{ch} s}{s + w_{ch}} = \frac{K_{ch} s}{s + w_{ch}} \tag{3.75}$$

whereupon the equivalent state space model is given as:

$$\begin{aligned} \dot{U}_s &= \left[-w_{ch} \right] U_s + \left[K_{ch} \right] \dot{x}_1 \\ y &= \left[1 \right] U_s \end{aligned} \tag{3.76}$$

As described in Section 3.6.2.1 the change of input signals applies here aswell, where one can identify the state space system as an ordinary differential equation.

R_{ch}	$800\,K\Omega$
C_{ch}	$1\,\mu F$
f_{cut}	$0.1918\,Hz$
w_{ch}	$1.25\,1/s$
S_s	$0.0042\,C/m$
K_{ch}	5.21×10^3

Table 3.8: Related constants, charge amplifier

3.6.2.3 Charge amplifier with zero offset

In [13] it was suggested to extend the aforementioned charge amplifier to meet the problem of DC offsets. Equivalent circuit schematics are given in Figure 3.14. Omitting the block $C(s)$ the feedback gain tries to nullify the applied voltage V_q to the output V_o. Referring to [13] the circuit is driven within the bandwidth, $q_l = V_q C_s$ and the charge amplifier has a gain given by $Z_s(s)$ only. Control issues for the charge amplifier seem obvious, as good tracking performance and DC regulation at low frequencies is required. The transfer function of interest appears to be between the applied voltage V_q and the output voltage V_o. For capacitive loads $Z_s(s) = \frac{1}{C_s s}$, $Z_l(s) = \frac{1}{C_l s}$ and under the assumption of neglecting the time constant of the op-amp output resistor together with the capacitance, the voltages

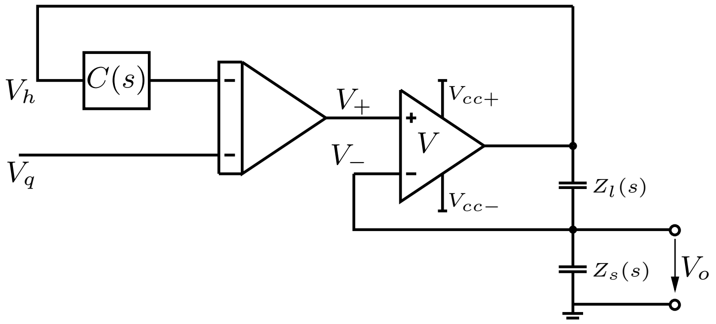

Figure 3.14: Schematics of the charge amplifier with zero offset

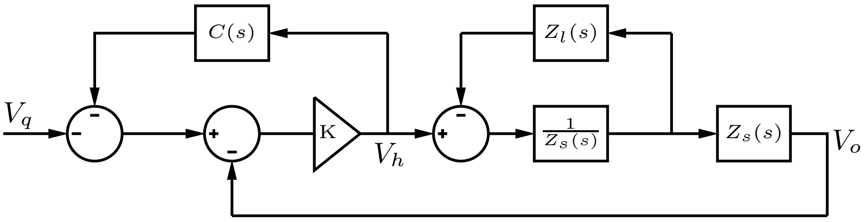

Figure 3.15: Block diagram of the charge amplifier with zero offset

V_o and V_h appear as:

$$V_o = V_h \frac{C_l}{(C_l + C_s)} \tag{3.77}$$

$$V_h = \frac{-(V_q + V_o) K}{(1 + KC(s))} \tag{3.78}$$

By inserting (3.78) in (3.77) the total transfer function can be written as:

$$\frac{V_o(s)}{V_q(s)} = \frac{-KC_l}{(1 + KC(s))(C_l + C_s) + KC_l} \tag{3.79}$$

The controller is designed as a simple integral controller $C(s) = \frac{\alpha}{s}$. For such a circuit no tuning is required but the circuit nullifies the DC offset automatically. Figure 3.16 shows an adaption of the DC offset. Additionally to that, the results from Section 3.5.2 where an LMS algorithm is used are presented as well. It happens that the LMS implementation converges a bit slower but eventually both methods find the correct offset. After convergence time, experiments show perfect tracking performance at complete suppression of DC offsets. The circuit, as schematically given in Figure 3.14, is assembled with simple operation amplifier wirings (integrator, inverter, subtractor) which can be found e.g. in [31]. A detailed circuit layout is given in Appendix B. Resistors are chosen in the range from $1K\Omega$ to $100K\Omega$ whereas capacitors are $47nF$ to $1\mu F$. A good value for α could be around ≈ 0.001.

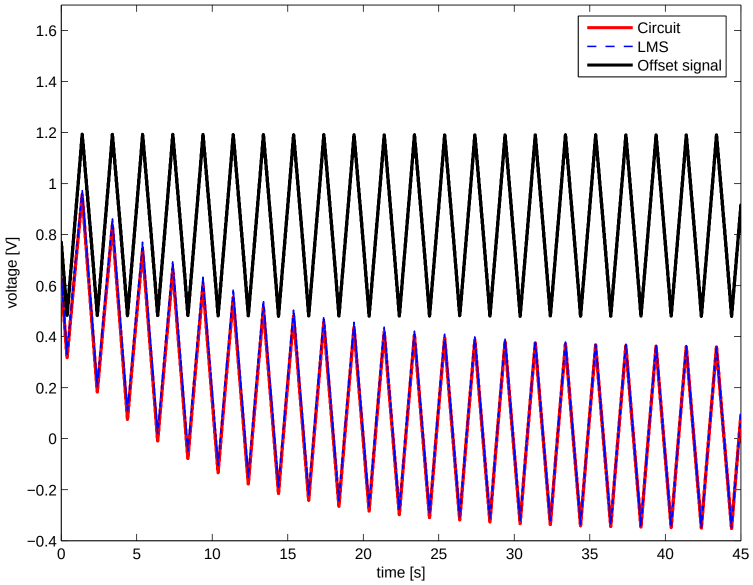

Figure 3.16: Adaption of the DC offset for an LMS and a circuit implementation

3.7 Piezovoltage-amplifier model

To deflect a piezoelectric tube in the range of some μm a voltage in the range of hundreds of volts is necessary. Of course this depends on the different PZTs in use, but still the voltage input needs to provide considerably high voltages. This circumstance requires a good and precise voltage amplifier, which should be linear and also work at high frequencies. Specifications of the amplifier in use, name the bandwidth with more than 200kHz. Simple frequency analysis in the lab verify this, when the amplifier is unloaded. However the frequency response changes as soon as a load is applied. In a first approximation one can assume the response to be of the first order. Additionally the frequency response changes as soon as the load is changed. Tests show a dependency between capacitive load and bandwidth. This relation suggests to imply that the transfer function of the amplifier is dependent on the load. Such a description makes the transfer function more versatile with respect to changes in the capacitance of a PZT. To evaluate and determine the generally valid transfer function, several tests with different loads were accomplished. The higher the load becomes, the lower the cut-off frequency is. In Figure 3.17 a frequency response plot shows the load dependence, the corresponding values are tabulated in 3.9.

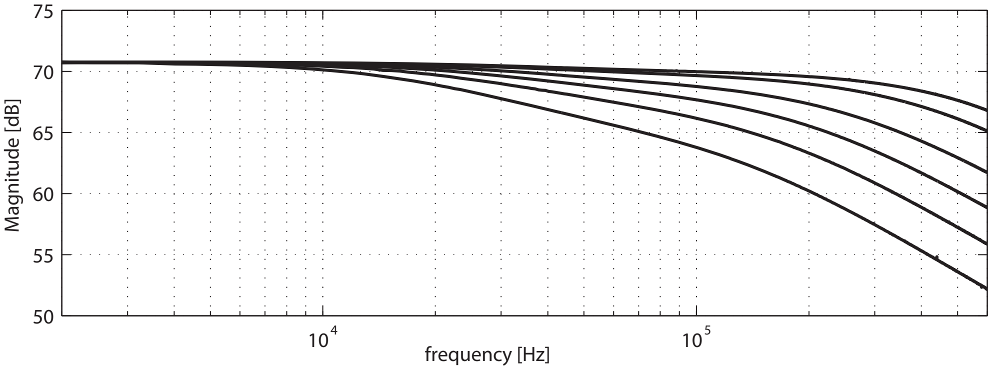

Figure 3.17: Frequency response with different capacitive loads

cut-off frequency $[Hz]$	capacitance load $[nF]$
5×10^4	100
6×10^4	81
8×10^4	60
1.2×10^5	47
2×10^5	25
3×10^5	16

Table 3.9: cut-off frequency versus load capacitance

Evaluation of the data above gives a formula for the cut-off frequency and the transfer function respectively:

$$f_{amp} = \frac{1}{200C}[Hz] \tag{3.80}$$

$$\frac{U_a}{U_{dsp}} = V_{gain}\frac{2\pi f_{amp}}{s + 2\pi f_{amp}} = \frac{b_a}{s + a_a} \tag{3.81}$$

Observe that for this application $C = C_{pzt}$ where C_{pzt} is assumed as constant. Subsequent to that the cut-off frequency is given as constant too. The transfer function is defined as the relation between the amplifier output and the input, which is typically given by the *dSpace* module and can either be a control signal or a predetermined waveform. As a state space model is required for establishing a total PZT-system model, one can define the amplifier dynamics in state space form as:

$$\begin{aligned}\dot{U}_a &= \begin{bmatrix}-a_a\end{bmatrix} U_a + \begin{bmatrix}b_a\end{bmatrix} U_{dsp} \\ y &= \begin{bmatrix}1\end{bmatrix} U_a\end{aligned} \tag{3.82}$$

C_{pzt}	$13\, nF$
f_{amp}	$300\, kHz$
w_{amp}	$1.885 \times 10^6\, 1/s$
V_{gain}	20
K_{amp}	3.76×10^7

Table 3.10: Related constants, piezovoltage amplifier

Chapter 4

Merged system model

In the course of this chapter a total system description of the piezoelectric actuator is set up. The goal is to fit the separate parts discussed in Chapter 3 into one single state space model. This includes the sensor dynamics, the amplifier dynamics and the PZT hysteresis effect as well as the mechanical PZT model itself. At first an electromechanical model is set up to combine mechanical and hysteresis effects. Later on the additional dynamics of sensors and the amplifier are added.

4.1 Electromechanical model

4.1.1 Physical background

The piezoelectric tube action is based on the piezoelectric effect as described in Chapter 2 (See also [28] for more information). The dielectric material is technically speaking an insulator, thus a relation between electric charge and voltage can be found. Additionally to the relations described by the dielectric effect, another mechanical relation arises when considering the conversion of the applied force to an expansion in length. Consider Figure 4.1 which displays the changing physical domain within a piezoelectric actuator.

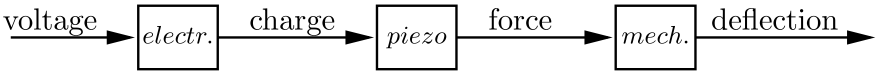

Figure 4.1: Block diagram of the physical relations in a piezoelectric actuator

From those observations one can see the piezoelectric effect as a directive of combining the electrical and mechanical domains.

4.1.2 Hysteresis interrelation

In [24] it was found that there clearly is a hysteresis relation between the applied voltage and the deflection as well as between the applied voltage and the charge. In contrast to that, a quite linear relation could be detected between the charge and the deflection. A possible explanation may be found in the constitutive relations for piezoelectricity (3.64). In a first approximation one can assume the mechanical stress T to be ≈ 0 compared with the stalling force, which yields the relation:

$$S = dE \tag{4.1}$$

$$D = \epsilon_0 E + P \tag{4.2}$$

ϵ_0 is the natural dielectric permittivity and P the polarisation of the ceramic material. The piezoelectric ceramic, which is ferroelectric, shows a hysteresis like relation between P and E. This is achieved via a high polarising field in the final stage of the manufacturing process, which causes the ceramic to remain in a remanent polarisation. Ionic movement within the ceramic leads to a change in polarisation and is closely related to the piezoelectric strain. Regarding to the hysteresis between the electric field E and the polarisation P one can expect a hysteresis like relation between the piezoelectric strain and E.

Measurements approved the theory and corresponding plots are illustrated in Figure 4.2. A moderately linear relation between the charge and the deflection shows Figure 4.2(a). The relation between the applied voltage and the charge is already illustrated in Figure 3.7 when the hysteresis model parameters were estimated. Figure 4.2(b) displays the overall relation (applied voltage against displacement), which of course shows nonlinear behaviour as well as this is just a combination of the two aforementioned relations.

4.1.3 Model schematics

In [19] a quite accurate model was proposed to simulate the overall characteristics of a piezoelectric actuator. This model was adapted for the lab setup and is given in a slightly different form in Figure (4.3). For this purpose the hysteresis and piezo effect are separated. The voltage drop due to hysteresis effects is U_h (which is also dependent on the charge q) whereas the total applied voltage is U_a. The reverse piezoelectric effect transforms electrical domains into mechanical ones, which is realized by a simple factor

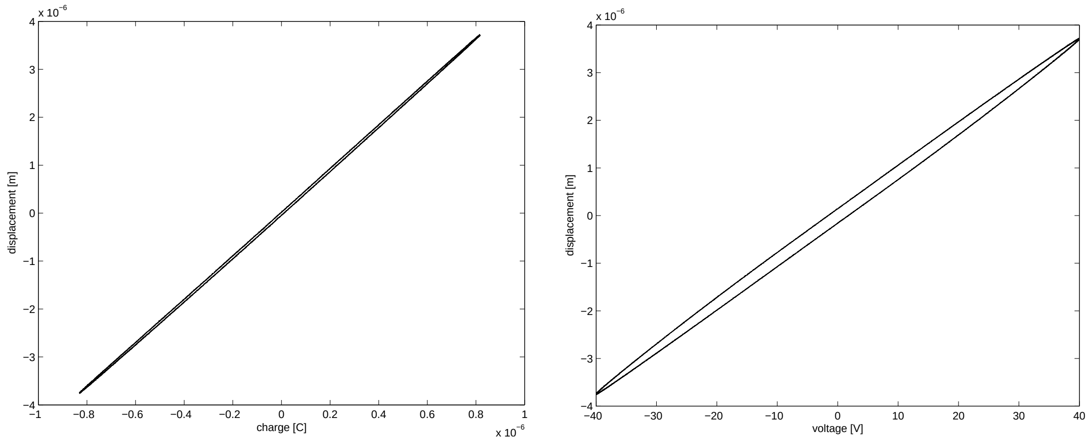

(a) (b)

Figure 4.2: Almost linear relation between charge and displacement (a), Nonlinear relation between applied voltage and displacement (b)

n. Factor C is the present capacitance induced by the dielectric material itself. The total current flowing through the circuit is $\dot{q}$ where $\dot{q}_p$ can be seen as the derivation of the charge from the mechanical side. However F_p is the transduced force on the electrical side. The relation between the force F_p and the deflection x is given by the dynamical model F_{em}. Consider also the relation of equal electrical and mechanical energy $U_t\, q_p = F_p\, x$.

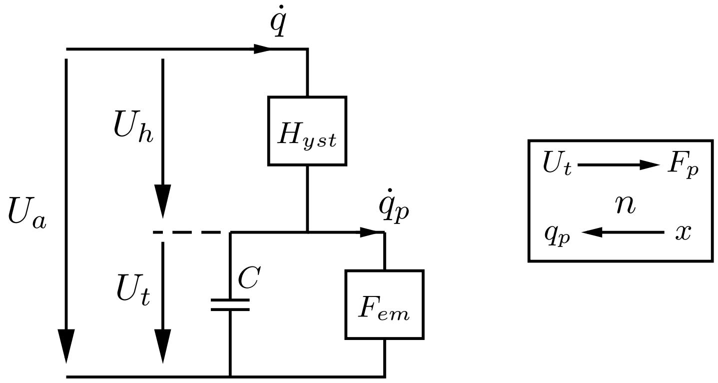

Figure 4.3: Electromechanical model of a piezoelectric actuator

Subsequently the set of electromechanical equations for a piezoelectric actuator appears to be:

$$U_a = U_h + U_t \tag{4.3}$$

$$q = H_{yst}(U_h) \tag{4.4}$$

$$q = n\,x + C\,U_p \tag{4.5}$$

$$F_p = n\,U_t \tag{4.6}$$

$$x = F_{em}(F_p) \tag{4.7}$$

Charge q is determined twice, once by the nonlinearity of the hysteresis (as a function of U_h) and the other time by the parallel branch with $q = q_c + q_p$ (Compare Figure (4.3)). It is composed of $q_c = C\,U_t$ and q_p. The operators H_{yst} and F_{em} have been part of the discussion in Section 3.2 and 3.3 and represent the hysteresis model and the mechanical model respectively. Displayed in block diagram order, the overall electromechanical system can be considered as follows:

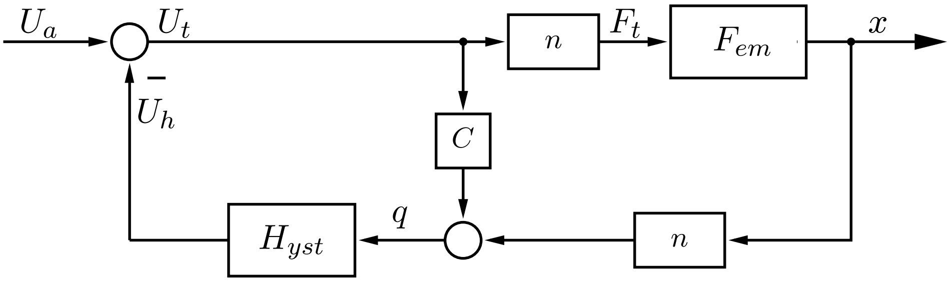

Figure 4.4: Flow diagram of the PZT electromechanical model

4.2 Linear model

In a first step the system is modelled as a linear model. A good approximation for modelling an actuated PZT, can be achieved by connecting the part models from Chapter 3. Considering linear relationships only, the hysteresis model is not taken into consideration but rather a transfer function between the input voltage and the displacement is taken into account. In details the state space models from (3.17), (3.73), (3.59) and (3.82) yield to one total system description:

$$\begin{bmatrix} \dot{U_a} \\ x_1 \\ x_2 \\ U_c \\ U_s \end{bmatrix} = \begin{bmatrix} -a_a & 0 & 0 & 0 & 0 \\ 0 & 0 & 1 & 0 & 0 \\ b_{lin} & -a_0 & -a_1 & 0 & 0 \\ 0 & K_c & 0 & -w_c & 0 \\ 0 & 0 & K_s & 0 & -w_s \end{bmatrix} \begin{bmatrix} U_a \\ x_1 \\ x_2 \\ U_c \\ U_s \end{bmatrix} + \begin{bmatrix} b_a \\ 0 \\ 0 \\ 0 \\ 0 \end{bmatrix} U_{dsp}$$

$$y = \begin{bmatrix} 0 & 0 & 0 & 1 & 0 \\ 0 & 0 & 0 & 0 & 1 \end{bmatrix} \begin{bmatrix} U_{amp} \\ x_1 \\ x_2 \\ U_c \\ U_s \end{bmatrix} \tag{4.8}$$

The variable x_1 stands for the tube's displacement whereas U_c and U_s is the capacitive and strain sensor signal respectively. One can notice an inappropriate transfer function $\frac{q(s)}{x_1(s)}$ for the mechanical model as now the only input is the applied voltage. Because this model deals with linear equations only, the relation between applied voltage/ charge is assumed linear as well and entered in the corresponding function. Parameter b_{lin} appears then to be $b_{lin} = 3.02$. Preceding investigations concerning the linear Kalman filter (Section 5.1) are treated with discrete time models. To do so the continuous model has to be discretised. A very rough approximation is given in (4.9) whereas within implementations the MATLAB function **c2d** has been used for this conversion.

$$\begin{bmatrix} U_a \\ x_1 \\ x_2 \\ U_c \\ U_s \end{bmatrix}_{k+1} = \begin{bmatrix} 1-Ta_a & 0 & 0 & 0 & 0 \\ 0 & 1 & T & 0 & 0 \\ Tb_{lin} & -Ta_0 & 1-Ta_1 & 0 & 0 \\ 0 & TK_c & 0 & 1-Tw_c & 0 \\ 0 & 0 & TK_s & 0 & 1-Tw_s \end{bmatrix} \begin{bmatrix} U_a \\ x_1 \\ x_2 \\ U_c \\ U_s \end{bmatrix}_k + \begin{bmatrix} T\left(1-Ta_a\right)b_a \\ 0 \\ T^2 b_{lin} b_a \\ 0 \\ 0 \end{bmatrix} U_{dsp,k}$$

$$y_k = \begin{bmatrix} 0 & 0 & 0 & 1 & 0 \\ 0 & 0 & 0 & 0 & 1 \end{bmatrix} \begin{bmatrix} U_{amp} \\ x_1 \\ x_2 \\ U_c \\ U_s \end{bmatrix}_k \tag{4.9}$$

4.3 Nonlinear model

In a second and more sophisticated step the system is modelled as a nonlinear system by taking the hysteresis effects into account. Therefore (4.4) - (4.7) are rewritten to be appropriate for state space expression. Again the part models given in (3.17), (3.73), (3.59), (3.30) and (3.82) are used to configure the overall system model. By simply inserting the different transfer functions the model appears to be:

$$
\begin{aligned}
\dot{\begin{bmatrix} U_a \\ U_h \\ x_1 \\ x_2 \\ U_c \\ U_s \end{bmatrix}} &= \begin{bmatrix} -U_a\, a_a + U_{dsp} b_a \\ f\left(\dot{U_h}\right) \\ x_2 \\ U_a\, b_0\, n - U_h\, b_0\, n - x_1\, a_0 - x_2\, a_1 \\ x_1\, K_c - U_c\, \omega_c \\ x_2\, K_s - U_s\, \omega_s \end{bmatrix} \\
y &= \begin{bmatrix} 0 & 0 & 0 & 0 & 1 & 0 \\ 0 & 0 & 0 & 0 & 0 & 1 \end{bmatrix} \begin{bmatrix} U_a \\ U_h \\ x_1 \\ x_2 \\ U_c \\ U_s \end{bmatrix}
\end{aligned}
\tag{4.10}
$$

The function $f(\dot{U_h})$ depends on the sign of $\dot{U_h}$ and is defined as given below:

$$
f(\dot{U_h}) = \frac{n\, x_2 + C\,(U_{dsp}\, b_a - U_a a_a)}{b + C + \alpha U_h\,(a + C) - \alpha n x_1 - \alpha C U_a} \quad \text{for } \dot{U_h} > 0 \tag{4.11}
$$

and

$$
f(\dot{U_h}) = \frac{n\, x_2 + C\,(U_{dsp}\, b_a - U_a a_a)}{b + C - \alpha U_h\,(a + C) + \alpha n x_1 + \alpha C U_a} \quad \text{for } \dot{U_h} < 0 \tag{4.12}
$$

During simulation and implementation tests, the system model as given above turned out to be quite complex. It clearly does simulate the system behaviour in an excellent way, but complexity turns out to be a problem. Due to this another, simplified, but still nonlinear model was consulted. This new model is based on the relations given in (4.4)-

(4.7) and only slight changes are made. The model is redefined under the assumption that the charge, which is given by the nonlinear hysteresis (3.31) is the input of the mechanical model. The mechanical model itself, with charge as the input and displacement as the output, is again given by (3.17). With respect to this simplified combination of dynamics the new state space form is given as:

$$\dot{\begin{bmatrix} U_a \\ q \\ x_1 \\ x_2 \\ U_c \\ U_s \end{bmatrix}} = \begin{bmatrix} -U_a\, a_a + U_{dsp} b_a \\ \alpha\, a\, \left| U_{dsp} b_a - U_a\, a_a \right| \, U_a - \alpha\, \left| U_{dsp} b_a - U_a\, a_a \right| \, q + b\, \left(U_{dsp} b_a - U_a\, a_a \right) \\ x_2 \\ q\, b_0 - x_1\, a_0 - x_2\, a_1 \\ x_1\, K_c - U_c\, \omega_c \\ x_2\, K_s - U_s\, \omega_s \end{bmatrix}$$

$$y = \begin{bmatrix} 0 & 0 & 0 & 0 & 1 & 0 \\ 0 & 0 & 0 & 0 & 0 & 1 \end{bmatrix} \begin{bmatrix} U_a \\ q \\ x_1 \\ x_2 \\ U_c \\ U_s \end{bmatrix} \tag{4.13}$$

With almost the same simulation results, this simplified model causes less problems when it comes to implementation issues. Thus further investigations and extended Kalman filtering are related to this model.

Chapter 5

Kalman filter

For linear systems the Luenberger observer is a well known tool to estimate unreachable system states. The theory behind that is that the observer has just to copy the system and place the intrinsic value on specified points. The fact that input-, output- and state noise influence the system are not accounted for in that observer, which makes the vector state estimation more inaccurate. One can ask how we can still get an optimal prediction of such system states. This can be answered with the theory of the Kalman filter. The linear Kalman filter is, with respect to stochastic noise parameters, designed to yield an optimal state prediction. This kind of Kalman filter, which is mainly used to estimate system states, can even be extended so as to account for changes in the system itself. This is then called the *extended* Kalman filter. As the Kalman filter is mainly implemented in discrete form, the model found in Section 4.3 is used as a reference model in the following.

5.1 Linear Kalman filter

5.1.1 Theory about the Kalman filter

The discrete linear model found in Section 4.3 was used to implement the linear Kalman filter. To meet the Kalman filter specifications the linear model has to be extended with the input and output noise. Under further constraints

- the PZT tube displacement is constant over a sampling time period
- the sampling period is constant

the following LTI model can be deduced:

$$\begin{aligned} x_{k+1} &= \mathbf{\Phi} x_k + \mathbf{H} u_k + w_k \\ y_k &= \mathbf{C} x_k + v_k \end{aligned} \tag{5.1}$$

The vectorial stochastic processes w_k (state noise) and v_k (output noise) are depicted to be stationary white noise and uncorrelated. In [5] the Kalman filter equations for model (5.1) emerge to:

$$\begin{aligned} x_k^* &= \mathbf{\Phi} \hat{x}_{k-1} + \mathbf{H} u_{k-1} \\ \mathbf{P}^*{}_k &= \mathbf{\Phi} \mathbf{P}_{k-1} \mathbf{\Phi}^T + \mathbf{Q} \\ \mathbf{K}_k &= \mathbf{P}_k^* \mathbf{C}^T \left(\mathbf{C} \mathbf{P}_k^* \mathbf{C}^T + \mathbf{R} \right)^{-1} \\ \hat{x}_k &= x_k^* + \mathbf{K}_k \left(y_k - \mathbf{C} x_k^* \right) \\ \mathbf{P}_k &= \left(\mathbf{E} - \mathbf{K}_k \mathbf{C} \right) \mathbf{P}_k^* \end{aligned} \tag{5.2}$$

The covariance matrix $\mathbf{Q}$ results in:

$$\mathbf{Q} = \mathbf{H}\, \mathbf{Q}_u\, \mathbf{H} \tag{5.3}$$

The covariance matrix $\mathbf{Q}_u$ is considered to be the input noise matrix. Additional to that it is weighted by the input matrix $\mathbf{H}$. That is why $\mathbf{H}$ is often also called weighting matrix . $\mathbf{R}$ is defined to be the covariance matrix of the output noise. The Kalman filter equations (5.2) describe a recursive calculation specification. For the start up at $(k = 0)$ the equations for $\hat{x}_k$ and $\mathbf{P}_k$ are not defined. By reason of that the variables x_k^* and $\mathbf{P}^*{}_k$ have to be well defined in advance to get the Kalman filter going. The variable x_k^* has been introduced as the predicted estimate value without any consideration of measurements. With that knowledge we find the best estimation for x_0^* to be exactly the expected value of x_0.

$$x_0^* = E\left(x_0\right) = m_0 \tag{5.4}$$

The matrix $\mathbf{P}^*{}_k$ has been assumed to be the covariance matrix of the error of the predicted estimate value. This yields us to the following:

$$\begin{aligned} \mathbf{P}^*{}_0 &= E\left\{(x_0^* - x_0)(x_0^* - x_0)^T\right\} \\ &= E\left\{(m_0 - x_0)(m_0 - x_0)^T\right\} \end{aligned} \tag{5.5}$$

Initial states for the PZT actuator are all assumed to be 0. For the P_0^*-matrix an appropriate choice with fairly possible values is advisable but one can note that this choice is not highly important for the estimation performance.

$$x_0^* = \begin{bmatrix} 0 & 0 & 0 & 0 & 0 \end{bmatrix} \qquad \mathbf{P}^*{}_0 = \begin{bmatrix} \epsilon & 0 & 0 & 0 & 0 \\ 0 & \epsilon & 0 & 0 & 0 \\ 0 & 0 & \epsilon & 0 & 0 \\ 0 & 0 & 0 & \epsilon & 0 \\ 0 & 0 & 0 & 0 & \epsilon \end{bmatrix} \tag{5.6}$$

Aside from that, a good choice of the matrices $\mathbf{Q}$ and $\mathbf{R}$ is evident to achieve a satisfying performance. Considering the equations listed in (5.2) equation 2,3 and 5 comprise calculations for the Kalman gain $\mathbf{K}_k$. Especially equation 3 is very compute intensive as the inverse of a matrix has to be calculated. Merging the equations given in (5.2) the simulation block diagram given in Figure 5.1 is supposed. The input noise is mainly caused by some finite resolution of the ADC. The input noise variance can be determined via the

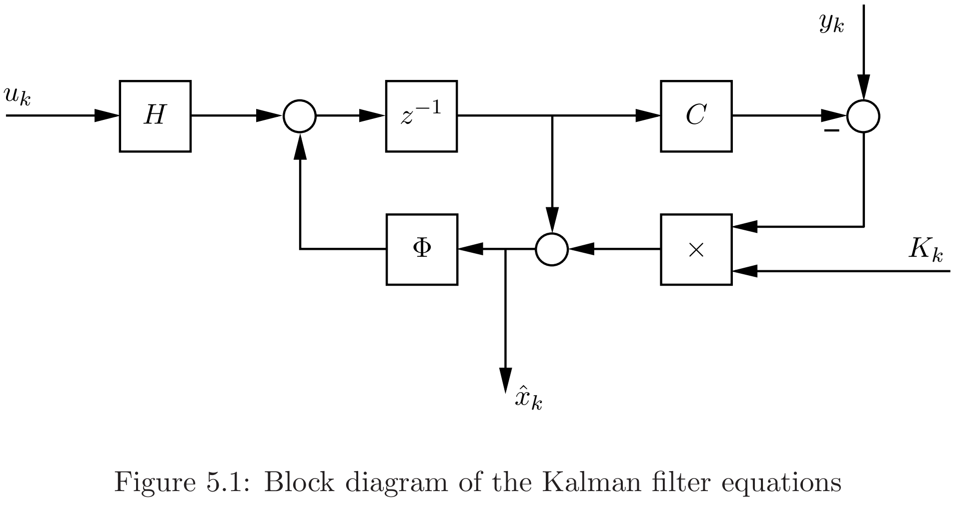

Figure 5.1: Block diagram of the Kalman filter equations

operating limit (±10) and the resolution ($16\,bit$).

$$LSB = \frac{20}{2^{16}} \qquad \sigma_w = \frac{LSB}{\sqrt{16}} \tag{5.7}$$

An evaluation of the output noise signal gives the corresponding variance (Compare Section 5.1.2). Assuming that the input noise as well as the output noise are white noise, the covariance matrices $\mathbf{Q}_u$ and $\mathbf{R}$ happen to have diagonal entries only.

$$\mathbf{R} = \begin{bmatrix} \sigma_c^2 & 0 \\ 0 & \sigma_s^2 \end{bmatrix} \qquad \mathbf{Q} = \mathbf{H} \begin{bmatrix} \sigma_w^2 \end{bmatrix} \mathbf{H}^T \tag{5.8}$$

It should be mentioned that experimental adjustments showed an even better performance when the $\mathbf{R}$ matrix was slightly changed. For the last entry $\sigma_s^2 \times 0.7$ was chosen instead of σ_s^2. A possible reason to that could be some incorrect measurements when the standard deviation was determined.

5.1.2 Noise properties

To apply the ordinary Kalman filter as described in Section 5.1, according to [3] several properties have to be fulfilled. Partly already mentioned in Section 5.1.1 the Kalman filter requires the following noise properties:

1. **Stationary noise**
   Stationarity is given for both the strain and capacitive sensor noise. For display reasons the noise signal was averaged at every point over a window of 100 data points. Figure 5.2 illustrates the respective stationary noise signals.

2. **White noise**
   To prove the noise to be white, an autocorrelation seems appropriate. Only a peak at 0 indicates perfect white noise. This cannot be expected but a good approximation appears for both noise signals. According plots are found in Figure 5.3.

3. **Gaussian distributed noise**
   The Kalman filter gain is optimized for only one distribution peak. If two or more peak distributions appear, other solutions (like a particle filter) are more appropriate. The probability density functions (pdf) show roughly Gaussian distribution (Figure 5.4).

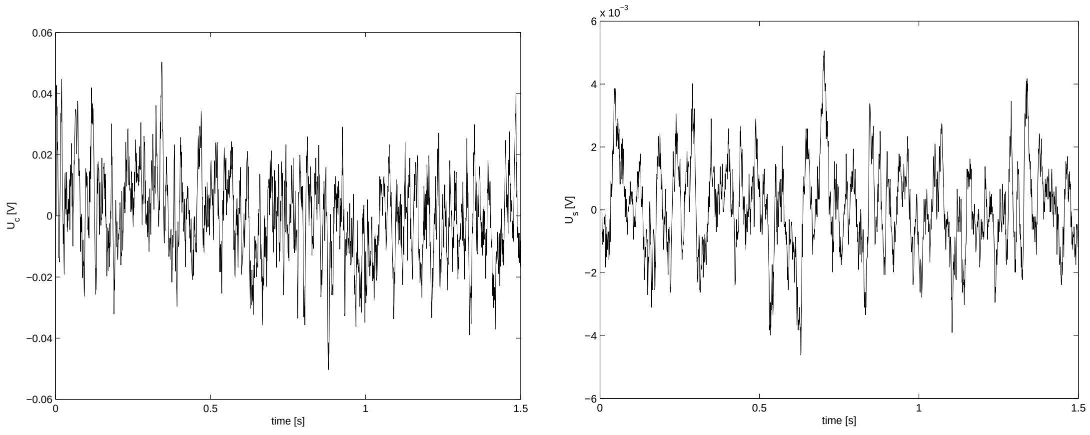

(a) (b)

Figure 5.2: Stationary noise for the capacitive sensor (a) and the strain sensor (b)

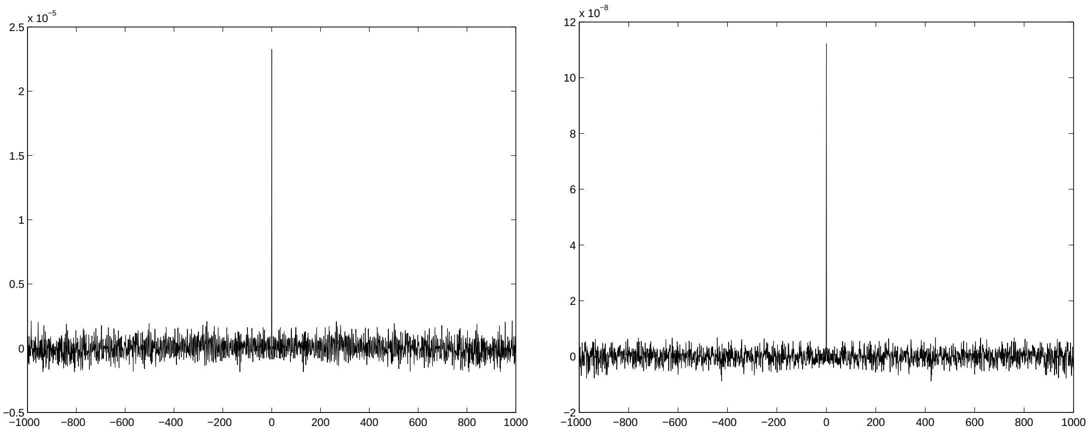

(a) (b)

Figure 5.3: Autocorrelation functions for (a) capacitive sensor noise and (b) strain sensor noise. Peaks at 0 indicate approximate uncorrelated signals.

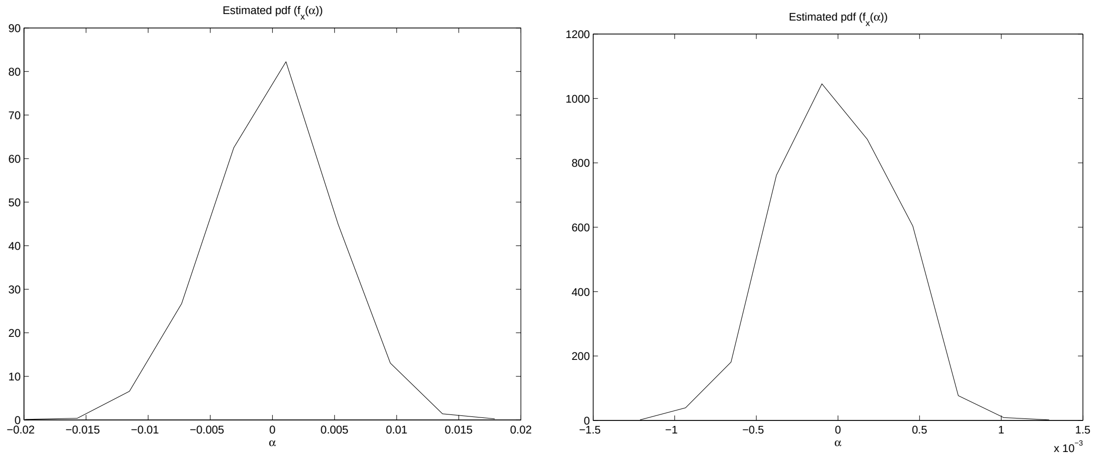

(a) (b)

Figure 5.4: Roughly Gaussian distribution for (a) capacitive sensor noise and (b) strain sensor noise.

The gained noise data is summed up in Table 5.1. The values for the different matrices within the linear Kalman filter implementation are summarized again in Table 5.2.

	cap. sensor	strain sensor
stationary	yes	yes
white noise	yes	yes
Gaussian distribution	approx.	approx.
standard deviation σ	5×10^{-3}	3.3×10^{-4}
mean value η	1.24×10^{-15}	3.01×10^{-19}

Table 5.1: Noise data

σ_c	σ_s	σ_w	ϵ
5×10^{-3}	3.3×10^{-4}	7.6×10^{-5}	0.1

Table 5.2: Summarized parameters for the linear Kalman filter

5.2 Extended Kalman filter

Section 5.1 dealt with linear system equations. This kind of system description does not pay attention to any nonlinear behaviour of the system. A positive consequence of that is that the convenience that the Kalman filter gains can be calculated in advance. Compare (5.2) and especially equation 2,3 and 5 which are completely isolated from x_k and y_k. The negative side becomes apparent when nonlinearities dominate the system. This makes it impossible to design a linear system description and therewith an appropriate Kalman filter. But exactly this problem is featured by the *extended* Kalman filter.

5.2.1 Theory about the extended Kalman filter

For nonlinear applications the Kalman filter theory can be used in 2 different ways. As the system must be linearized at some point, the question of where and how arise.

- Linearization about a nominal value. If these nominal values are already known in advance one can pre-compute the linearization along this trajectory. With this, another linearization during real time is not necessary and real time implementations become less computation intensive.
- Another way to operate a Kalman filter is to determine the trajectory during computation time. This means the system is linearized with regard to the actual state vector. An advantage of this method is, that only the state estimation error is included in the perturbation. As this error is usually smaller than the one of a nominal trajectory a better performance is obvious.
- A possibility to earn greater applicability is to also include second order terms. This results in a higher complexity in computation.

5.2.2 Nonlinear plant

In the following a continuous nonlinear system description as represented in (5.9) is used.

$$\begin{aligned} \dot{x} &= f(x,u,t) + w(t) \\ y(t) &= h(x,u,t) + v(t) \end{aligned} \tag{5.9}$$

where the noise related domains are:

Plant noise:	Measurement noise:
$\mathbf{E}\{w(t)\} = 0$	$\mathbf{E}\{v(t)\} = 0$
$\mathbf{E}\left\{w(t)w^T(s)\right\} = \delta(t-s)Q(t)$	$\mathbf{E}\left\{v(t)v^T(s)\right\} = \delta(t-s)R(t)$

Table 5.3: Comparison of errors depending on the order size

Implemented for the nonlinear PZT system is the linearization about the estimated trajectory. This means the Taylor series expansion is evaluated with regard to the estimated trajectory $\hat{x}(t)$. At each step in time a new linearized system description is calculated, which has to fulfil the condition of observability (explanations on that can be found in e.g.: [20]). The newly calculated linear matrices F, H are used to calculate the Kalman gain K and the covariance matrix P. A drawback of this is, as mentioned above the computation complexity.

5.2.3 Matrix definitions

The sensor signals appear to be the same, which gives the identical **R** matrix as stated in the linear Kalman filter description (5.8). Matrix **Q** can instead not be determined in the same intuitive way as before. The state variables appear to be different and a new matrix **G** is added to weigh the state noise (Compare (5.15)). The displacement and its derivation are assumed to have no noise. Noise for the states 'applied voltage U_{amp}' and 'charge q' can be determined with adequate measurements. All other state noises are set to 0. This yields the following state noise covariance matrix **Q**:

$$\mathbf{Q} = \begin{bmatrix} \sigma_u^2 & 0 & 0 & 0 & 0 & 0 \\ 0 & \sigma_q^2 & 0 & 0 & 0 & 0 \\ 0 & 0 & 0 & 0 & 0 & 0 \\ 0 & 0 & 0 & 0 & 0 & 0 \\ 0 & 0 & 0 & 0 & 0 & 0 \\ 0 & 0 & 0 & 0 & 0 & 0 \end{bmatrix} \tag{5.10}$$

Initial value definition is done in a similar way as within the linear model. Already mentioned before, is the influence of these initial values vanishing by the run of time. For the initial state values x_0^* and the initial covariance matrix $\mathbf{P^*}_0$ following values were chosen:

$$x_0^* = \begin{bmatrix} 0 & 0 & 0 & 0 & 0 & 0 \end{bmatrix} \qquad \mathbf{P^*}_0 = \begin{bmatrix} \lambda & 0 & 0 & 0 & 0 & 0 \\ 0 & \lambda & 0 & 0 & 0 & 0 \\ 0 & 0 & \lambda & 0 & 0 & 0 \\ 0 & 0 & 0 & \lambda & 0 & 0 \\ 0 & 0 & 0 & 0 & \lambda & 0 \\ 0 & 0 & 0 & 0 & 0 & \lambda \end{bmatrix} \tag{5.11}$$

The values for the different matrices within the extended Kalman filter implementation are summarized again in Table 5.2.3.

σ_c	σ_s	σ_u	σ_q	λ
5×10^{-3}	3.3×10^{-4}	3.1×10^{-5}	1.6×10^{-8}	0.1

Table 5.4: Summarized parameters for the extended Kalman filter

5.2.4 Extended Kalman filter equations

The relevant equations defining the EKF are summed up in (5.12-5.15) (Compare also [16]). A corresponding block diagram of a possible implementation is illustrated in Figure 5.5.

State estimation:

$$\dot{\hat{x}}(t) = f(\hat{x}, u, t) + K(t)\left[y(t) - \hat{y}(t)\right] \tag{5.12}$$

Measurement prediction:

$$\hat{y}(t) = h(\hat{x}, u, t) \tag{5.13}$$

Kalman gain equations:

$$\dot{P}(t) = F_1(t)P(t) + P(t)F_1(t) + G(t)QG^T(t) - K(t)R(t)K^T(t) \tag{5.14}$$

$$K(t) = P(t)H_1^T(t)R^{-1}(t) \tag{5.15}$$

Matrices $F_1(t)$ and $H_1(t)$ are the approximately linearized matrices of the functions $f(x, u, t)$ and $h(x, u, t)$ where Section 5.2.5 gives a more detailed explanation of calculation methodology.

5.2.5 Matrix evaluation

The EKF works as mentioned in the preceding chapter very similar to the linear Kalman filter. To guarantee such a functionality, linear matrices F and H have to be obtained at

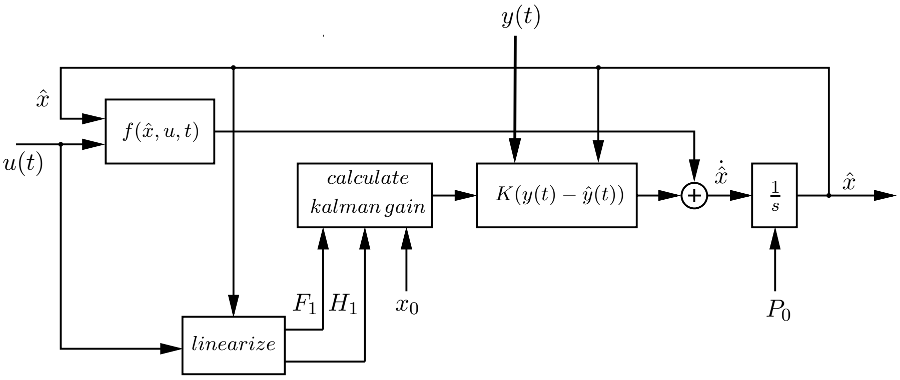

Figure 5.5: Block diagram of the extended Kalman filter

each time step. The linearization is done by evaluating the Jacobi matrices:

$$F_1(t) = \left.\frac{\partial f(x,u,t)}{\partial x(t)}\right|_{x=\hat{x}(t),u=u(t)} \tag{5.16}$$

$$= \left.\begin{bmatrix} \frac{\partial f_1}{\partial x_1} & \frac{\partial f_1}{\partial x_2} & \frac{\partial f_1}{\partial x_3} & \cdots & \frac{\partial f_1}{\partial x_n} \\ \frac{\partial f_2}{\partial x_1} & \frac{\partial f_2}{\partial x_2} & \frac{\partial f_2}{\partial x_3} & \cdots & \frac{\partial f_2}{\partial x_n} \\ \frac{\partial f_3}{\partial x_1} & \frac{\partial f_3}{\partial x_2} & \frac{\partial f_3}{\partial x_3} & \cdots & \frac{\partial f_3}{\partial x_n} \\ \vdots & \vdots & \vdots & \ddots & \vdots \\ \frac{\partial f_m}{\partial x_1} & \frac{\partial f_m}{\partial x_2} & \frac{\partial f_m}{\partial x_3} & \cdots & \frac{\partial f_m}{\partial x_n} \end{bmatrix}\right|_{x=\hat{x}(t),u=u(t)} \tag{5.17}$$

and

$$H_1(t) = \left.\frac{\partial h(x,u,t)}{\partial x(t)}\right|_{x=\hat{x}(t),u=u(t)} \tag{5.18}$$

$$= \left.\begin{bmatrix} \frac{\partial h_1}{\partial x_1} & \frac{\partial h_1}{\partial x_2} & \frac{\partial h_1}{\partial x_3} & \cdots & \frac{\partial h_1}{\partial x_n} \\ \frac{\partial h_2}{\partial x_1} & \frac{\partial h_2}{\partial x_2} & \frac{\partial h_2}{\partial x_3} & \cdots & \frac{\partial h_2}{\partial x_n} \\ \frac{\partial h_3}{\partial x_1} & \frac{\partial h_3}{\partial x_2} & \frac{\partial h_3}{\partial x_3} & \cdots & \frac{\partial h_3}{\partial x_n} \\ \vdots & \vdots & \vdots & \ddots & \vdots \\ \frac{\partial h_m}{\partial x_1} & \frac{\partial h_m}{\partial x_2} & \frac{\partial h_m}{\partial x_3} & \cdots & \frac{\partial h_m}{\partial x_n} \end{bmatrix}\right|_{x=\hat{x}(t),u=u(t)} \tag{5.19}$$

Chapter 6

Simulation and experiments

The focus of this chapter is the simulation and hardware implementation of both the linear and extended Kalman filter. Furthermore appropriate controller schemes will be presented and tested. A comparison between an uncontrolled and a controlled system will make the need of a controller, especially at higher frequencies, even more evident. Implementations of the estimators and controllers are done in the Real Time Workshop for MATLAB. A dSpace prototype system DS1103 DSP was used for hardware implementations.

6.1 Linear model simulation

6.1.1 Linear Kalman filter

One of the features of a Kalman filter is to estimate different state variables. Above that it also fulfils a filtering function and processes signals for further use.

Performance of the displacement estimator can be analysed and tested with different trajectory signals ranging from $170\,nm$ to $3.6\,\mu m$ at 0.5 and $50\,Hz$. Figure 6.3 and 6.4 illustrate the estimated displacement and the resulting capacitive sensor signal. Excellent performance can be observed for both plots at 5 and $50\,Hz$ for a displacement of $3.6\,\mu m$. Observing Figure 6.4, the meaning and use of a controller becomes indispensable (More on that in Section 6.1.2). If the displacement range is however minimized to a range of $170\,nm$, noise problems become more serious. Figure 6.1 demonstrates the filtering performance and the improved displacement signal. Above that, this implementation does not just estimate the displacement but also the capacitive and strain sensor signal. The excellent filtering performance for both sensor signals is shown in Figure 6.1.

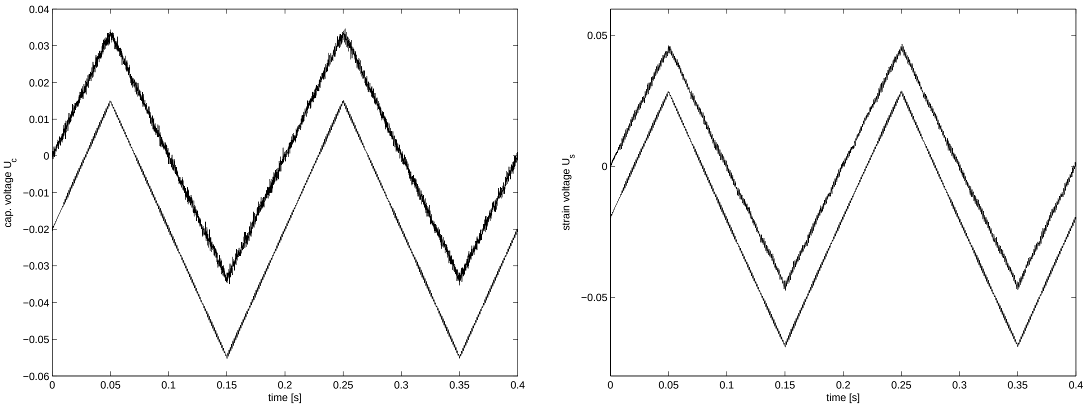

(a) capacitive sensor (b) strain sensor

Figure 6.1: Estimation results for the capacitive (a) and strain (b) sensor signal. Both plots show the measured signal (top) and the estimated equivalent (bottom). Additionally an offset was added for better clearness. Trajectory in use: $\pm 170\,nm$ at $5\,Hz$

6.1.2 Controller

In the preceding chapters emphasis was put on an appropriate form for a feasible controller design. In (4.9) the system is given in a convenient state space form where all the necessary states are estimated by means of the Kalman filter. As the sensor states are not needed for controlling, the system reduces to:

$$
\begin{aligned}
\begin{bmatrix} U_a \\ x_1 \\ x_2 \end{bmatrix}_{k+1} &= \begin{bmatrix} 1-Ta_a & 0 & 0 \\ 0 & 1 & T \\ Tb_{lin} & -Ta_0 & 1-Ta_1 \end{bmatrix} \begin{bmatrix} U_a \\ x_1 \\ x_2 \end{bmatrix}_{k} + \begin{bmatrix} T\left(1-Ta_a\right) b_a \\ 0 \\ T^2 b_{lin} b_a \end{bmatrix} U_{dsp,k} \\
y_k &= \begin{bmatrix} 0 & 1 & 0 \end{bmatrix} \begin{bmatrix} U_{amp} \\ x_1 \\ x_2 \end{bmatrix}
\end{aligned}
\tag{6.1}
$$

The number of different and advanced control designs seems endless but nevertheless the implementation of a state space controller is a good alternative both regarding performance and implementation. More exactly a state space controller with an integral part is implemented to get rid of an eventual steady state deviation from the desired value. For this purpose an integrator is added to the existing system which leads to the following form:

$$\begin{bmatrix} \mathbf{x} \\ \epsilon \end{bmatrix}_{k+1} = \begin{bmatrix} \Phi & 0 \\ \mathbf{C} & 0 \end{bmatrix} \begin{bmatrix} \mathbf{x} \\ \epsilon \end{bmatrix}_k + \begin{bmatrix} \mathbf{H} \\ 0 \end{bmatrix} u_k$$
$$y_k = \mathbf{C}\,\mathbf{x}_k \tag{6.2}$$

The control law appears then to be:

$$u_k := -\begin{bmatrix} h^T & h_I \end{bmatrix} \begin{bmatrix} \mathbf{x} \\ \epsilon \end{bmatrix}_k \tag{6.3}$$

After fine tuning, the poles were placed at 0.2 where both a good dynamic and overshoot behaviour could be observed. The total closed loop system including the Kalman filter, control gains and the system itself are illustrated in Figure 6.2.

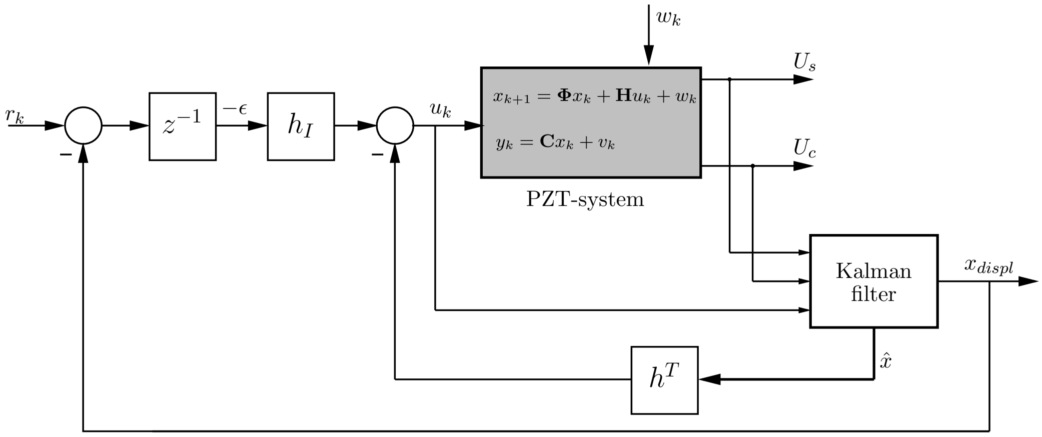

Figure 6.2: Block diagram of the controlled system

6.1.3 Comparison

For both the open and closed loop system appropriate experiments were conducted to present the filtering and estimating performance. The same desired trajectories were applied for both systems to guarantee genuine comparability. Clearly the results of the closed loop do not show any fluctuations as they are presented within the open loop results for higher frequencies. Results performed at $5\,Hz$ are illustrated in Figure 6.3. The same experiments at $50\,Hz$ are summarized in Figure 6.4.

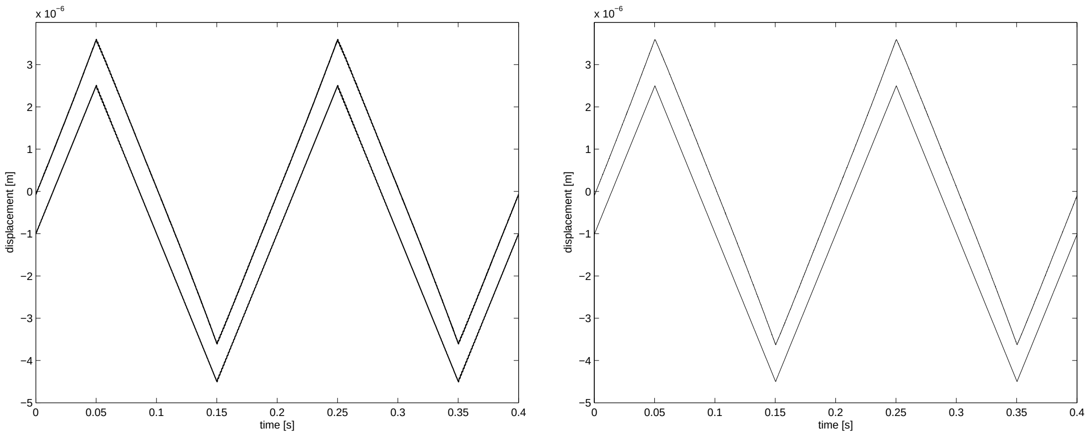

(a) open loop, range:±3.6 μm (b) closed loop, range:±3.6 μm

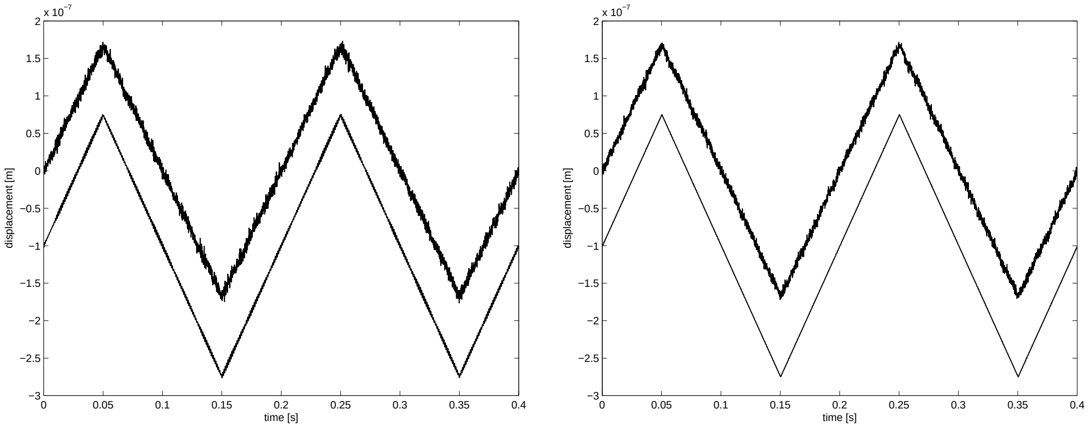

(c) open loop, range:±170 nm (d) closed loop, range:±170 nm

Figure 6.3: 5 Hz results for the open and closed loop system. Desired trajectories range from ±170 nm to ±3.6 μm. All the plots display the capacitive sensor signal (top) and the estimated displacement (bottom). For clarity an offset was added to the estimated states.

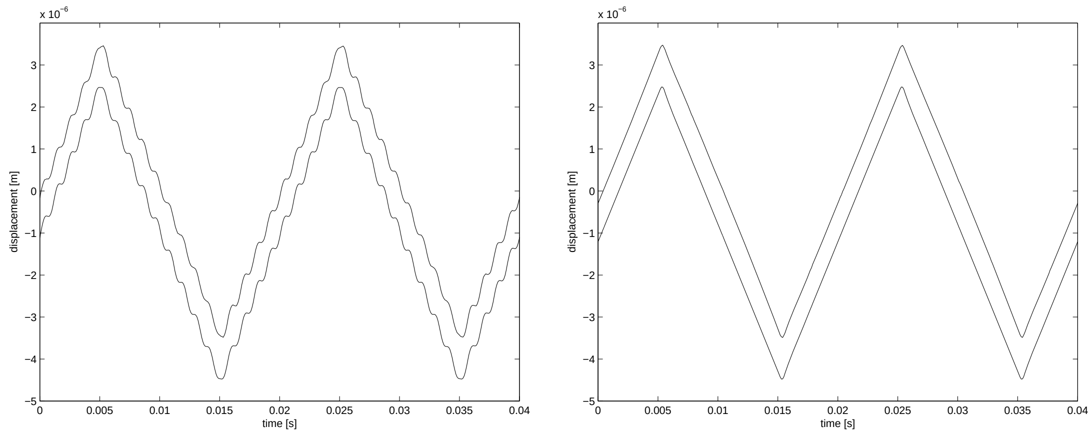

(a) open loop, range:±3.6 μm (b) closed loop, range:±3.6 μm

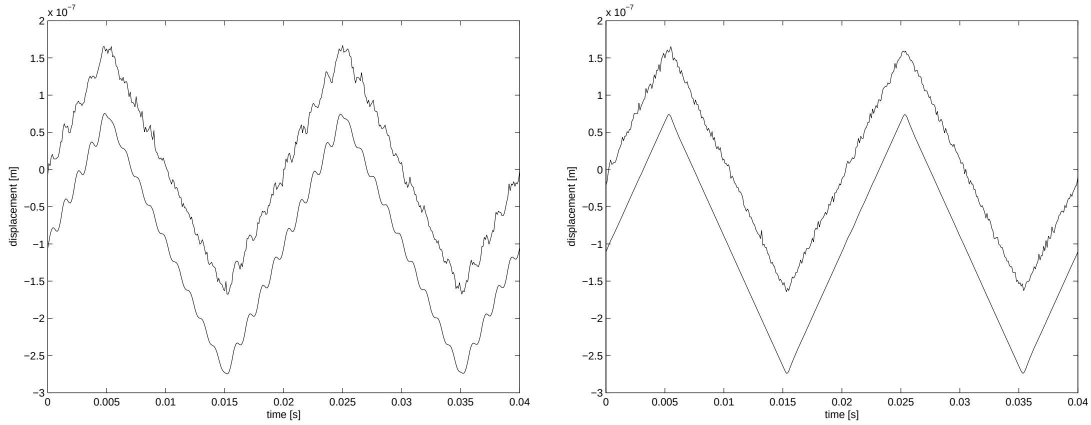

(c) open loop, range:±170 nm (d) closed loop, range:±170 nm

Figure 6.4: 50 Hz results for the open and closed loop system. Desired trajectories range from ±170 nm to ±3.6 μm. All the plots display the capacitive sensor signal (top) and the estimated displacement (bottom). For clarity an offset was added to the Kalman signal.

To numerically verify the resolution improvements, the tracking error has been calculated for the preceding experiments. Following to [2], the tracking error can be determined by calculating the rms difference of the displacement and a straight line over 90% of the full scan range. The measured capacitance displacement and the estimated displacement are evaluated and compared for different scan rates and ranges. The results for the open loop experiments are given in Table 6.1. At a lower scan rate (5 Hz) not modelled hysteresis effects sign for the error at 3.6 μm-range where noise dominates the error at 170 nm-range.

Vibrational effects at higher rates (50 Hz) cause then the higher tracking errors.

Open loop tracking error			
Frequency	Scan Range	RMS y_c	RMS x_1
5 Hz	170 nm	6.9 nm	2.4 nm
5 Hz	3.6 μm	7.28 nm	4.97 nm
50 Hz	170 nm	8.42 nm	5.88 nm
50 Hz	3.6 μm	127 nm	95 nm

Table 6.1: Open loop tracking error for different scan rates and displacement ranges.

Equivalent calculations were done for the closed loop experiments. The implemented controller provides improved performance for all ranges even at higher scan rates (50 Hz). The left tracking error is mostly caused by vibrational effects not coped by the controller. The calculated errors are given in Table 6.2.

Closed loop tracking error			
Frequency	Scan Range	RMS y_c	RMS x_1
5 Hz	170 nm	5.3 nm	0.4 nm
5 Hz	3.6 μm	5.28 nm	1.02 nm
50 Hz	170 nm	7.04 nm	2.28 nm
50 Hz	3.6 μm	76.4 nm	9.1 nm

Table 6.2: Closed loop tracking error for different scan rates and displacement ranges.

6.2 Nonlinear model simulation

6.2.1 Extended Kalman filter

The investigations described in Section 5.2 were implemented in the 'Realtime' Workshop as well. In the following the same experiments as listed in Section 6.1 were executed for the extended Kalman filter as well (Figure 6.7). Measurements for both the capacitive and strain sensor signal and their respective Kalman estimates are given in Figure 6.5. Similar to the linear implementation a good filtering performance is also obtained by the extended model.

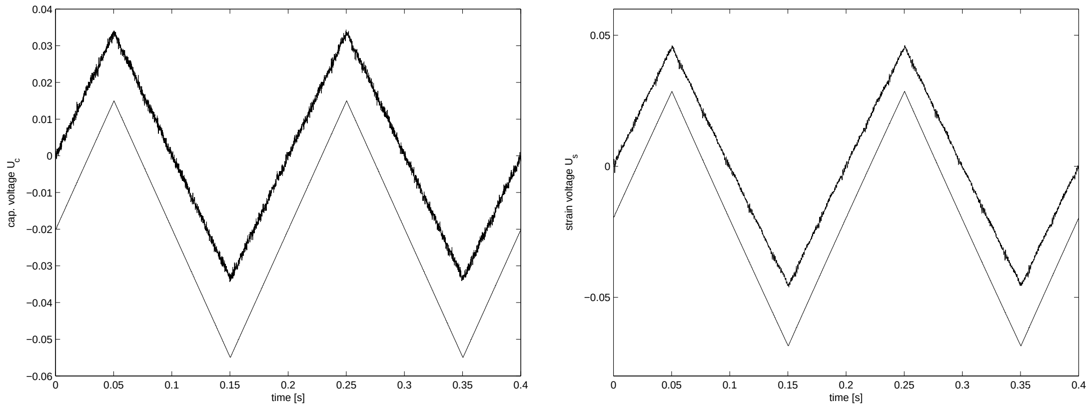

(a) capacitive sensor

(b) strain sensor

Figure 6.5: Estimation results for the capacitive (a) and strain (b) sensor signal. Both plots show the measured signal (top) and the estimated equivalent (bottom). Additionally an offset was added for better clearness. Trajectory in use: $\pm 180\,nm$ at $5\,Hz$

Another intention for the use of a Kalman filter was its ability of sensor fusion. The information provided by the two measurement signals should be utilized in an optimal way. These expectations in combination with the filtering features were sufficiently met and illustrated in Figure 6.6.

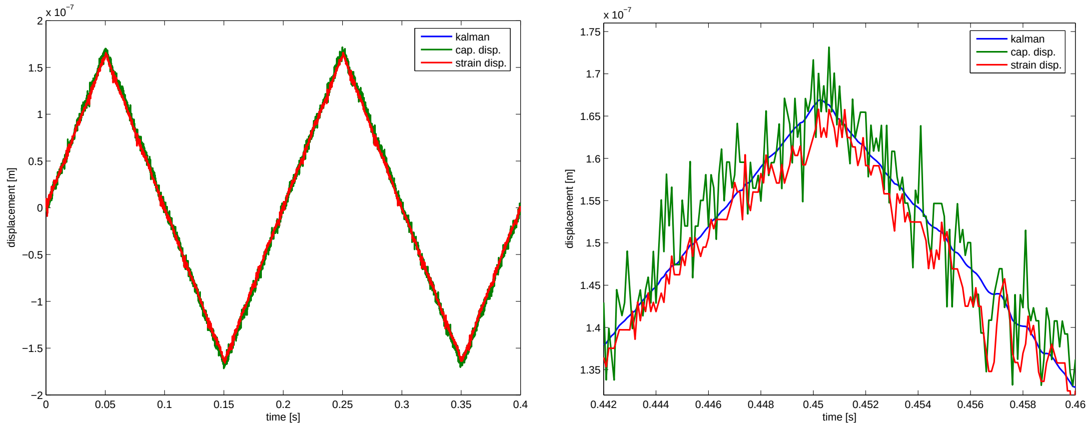

(a)

(b)

Figure 6.6: Sensor fusion done by the Kalman filter. (a) shows the total range. (b) is a zoomed area around the turning point.

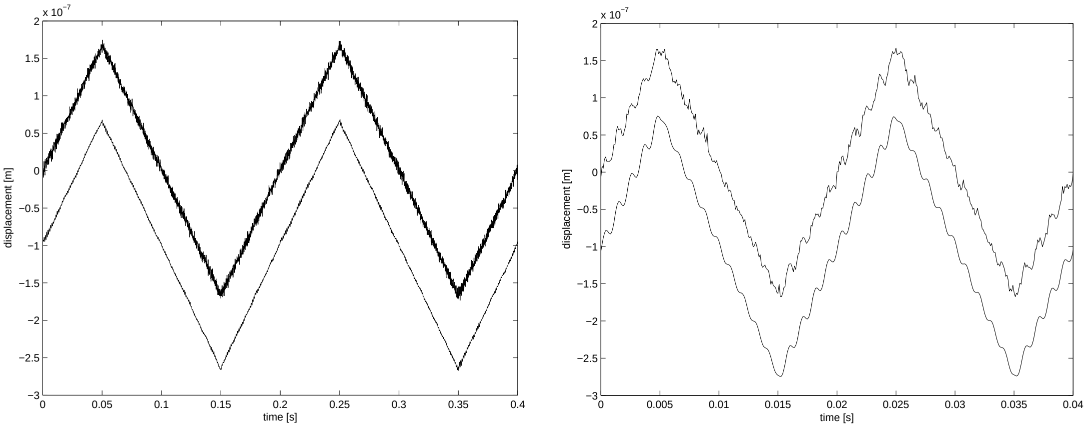

(a) range:±170 nm, rate:5 Hz

(b) range:±170 nm, rate:50 Hz

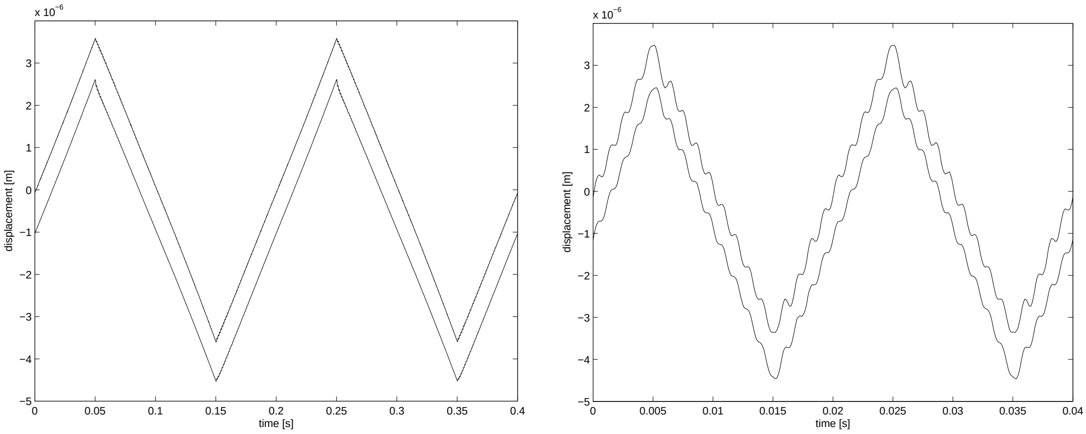

(c) range:±3.6 μm, rate:5 Hz

(d) range:±3.6 μm, rate:50 Hz

Figure 6.7: Results for the open loop systems. Desired trajectories range from ±170 nm to ±3.6 μm at a frequency of 5 Hz and 50 Hz. All the plots display the capacitive sensor signal (top) and the estimated displacement (bottom). For clarity an offset was added to the estimated states.

The tracking error evaluation is done in a similar way as suggested in Section 6.1.3. Hysteresis effects are now included in the model which does not change the error at small scan ranges (170 nm) or at higher rates (50 Hz) (Here the vibrational effects are dominating the error and not the hysteresis). The error at 5Hz at 3.6 μm scan range is again dominated by the hysteresis thus a better system model guarantees a lower tracking error (Compare the tracking error of the linear modle given in Table 6.1 at the same rate and range). In fact the error value is minimized but not dramatically which suggests further improvements in modelling the appearing nonlinear effects.

Open loop tracking error			
Frequency	Scan Range	RMS y_c	RMS x_1
5 Hz	170 nm	5.69 nm	1.9 nm
5 Hz	3.6 μm	6.98 nm	4.48 nm
50 Hz	170 nm	8.05 nm	4.9 nm
50 Hz	3.6 μm	132 nm	90 nm

Table 6.3: Open loop tracking error for different scan rates and displacement ranges. Nonlinear system

6.2.2 Controller

In the following a possible control scheme [7] is presented, which has been simulated with success but has not been tested in the lab so far. Therefore no guarantee of function can be given, but interesting design aspects for a hardware controller implementation are described and discussed.

6.2.2.1 Problem statement

The system of interest is already appropriate presented in (4.13). The sensor dynamics are now omitted as the system's transfer function is just from the voltage input to the displacement. For the sake of simplicity the system is rewritten in canonical form:

$$x^n + \sum_{i=1}^{r} a_i Y_i \left(x(t), \dot{x}(t), ..., x^{(n-1)}(t) \right) = b_0 \, w\left(v(t)\right) \tag{6.4}$$

where $w\left(v(t)\right)$ describes the nonlinearity with the applied voltage as an input and the charge as the output. (Compare also Figure 3.7). The objective is to find a control law for the input $v(t)$ in order that the systems' state vector $\mathbf{x} = [x \; \dot{x}]$ follows the desired trajectory $\mathbf{x}_d = [x_d \; \dot{x}_d]$ in the best possible way (e.g.: $\mathbf{x} \rightarrow \mathbf{x}_d$).

6.2.2.2 Adaptive control law

Following to (3.32) the hysteresis is expressed in a linear form with signal $v(t)$ and the boundary $d(v)$. Under consideration of this, the total system can be rewritten as:

$$x^n + \sum_{i=1}^{r} a_i Y_i \left(x(t), \dot{x}(t), ..., x^{(n-1)}(t) \right) = b_0\, av(t) + b_0\, d(v(t)) \tag{6.5}$$

resulting in a linear relation for the input $v(t)$. Restrictions are given by (3.34) and (3.35) which require a boundary such that:

$$||d(v)|| \leq \rho \tag{6.6}$$

In order to apply a suitable control law following assumptions are made:

- The mechanical model parameter b_0 has some known boundaries $[b_{0\,min} \quad b_{0\,max}]$.
- The hysteresis parameter a has some known boundaries $[a_{min} \quad a_{max}]$. a is defined as a design parameter for the hysteresis loop and determines the hysteresis slope. Under considerations of the adaption algorithm some good values for $[a_{min} \quad a_{max}]$ can be found.
- A new vector θ is defined and corresponds to $[(a_1/ba) \quad (a_0/ba)]$. From definitions above the boundaries can be defined as $[\theta_{min} \quad \theta_{max}]$.
- The boundary given in (6.6) is known.
- The desired trajectory $\mathbf{x}_d = [x_d \quad \dot{x}_d]$ is continuous and available.

For better understanding and easier writing the following definitions are made:

- $\tilde{\mathbf{x}}$ is the tracking error vector and defined as: $\tilde{\mathbf{x}} = \mathbf{x} - \mathbf{x}_d$
- $\hat{\theta}$ is an estimate of θ defined in assumption 2 above. $\tilde{\theta}$ is then the respective error $\tilde{\theta} = \hat{\theta} - \theta$.
- ϕ is defined as $\phi = (bc)^{-1}$ where $\hat{\phi}$ is again the estimate. The error is expressed as $\tilde{\phi} = \hat{\phi} - \phi$.

Furthermore the filtered tracking error is defined as:

$$s(t) = \left(\frac{d}{dt} + \lambda\right)^{(n-1)} \tilde{\mathbf{x}}(t) \tag{6.7}$$

$$s(t) = \Lambda^T \tilde{\mathbf{x}}(t) \qquad \text{with } \Lambda^T = [\lambda \quad 1] \tag{6.8}$$

Instead of driving the controller with the tracking error another 'tuning error' is introduced.

$$\mathbf{s}_\epsilon = \mathbf{s} - \epsilon\, sat\left(\frac{\mathbf{s}}{\epsilon}\right) \tag{6.9}$$

Parameter ϵ can be chosen arbitrary but positive. It should be noted that the tuning error disappears when the tracking error is smaller than the chosen ϵ. Under the aforementioned assumptions and abbreviations a control law for the system model given in (6.5) can be presented as follows:

$$\begin{aligned} v(t) &= -k_d\, \mathbf{s}(t) + \hat{\Phi}\, u_{fd}(t) + \mathbf{Y}^T(\mathbf{x})\hat{\Theta} - k_s\, sat\left(\frac{\mathbf{s}}{\epsilon}\right) && (6.10) \\ u_{fd}(t) &= \mathbf{x}_d^{(n)}(t) - \kappa^T \tilde{\mathbf{x}}(t) && (6.11) \\ \dot{\hat{\Theta}} &= Proj\left(\hat{\Theta}, -\gamma \mathbf{Y}(\mathbf{x})\mathbf{s}_\epsilon\right) && (6.12) \\ \dot{\hat{\phi}} &= Proj\left(\hat{\phi}, -\eta\, u_{fd}\, \mathrm{s}_\epsilon\right) && (6.13) \end{aligned}$$

For the $Proj.$-operators introduced above knowledge about some boundary values (given in the assumptions) is necessary. The operator Proj $\left(\hat{\theta}, -\gamma \mathbf{Y}(\mathbf{x})\mathbf{s}_\epsilon\right)$ is defined as follows:

$$Proj\left(\hat{\theta}, -\gamma \mathbf{Y}(\mathbf{x})\mathbf{s}_\epsilon\right) = \begin{cases} 0, & \text{if } \left[\hat{\theta}_i = \theta_{i\,max} \text{ and } \gamma\,(Y\,s_\epsilon)_i < 0\right] \\ -\gamma\,(Y\,s_\epsilon)\,, & \text{if } \left[\theta_{i\,min} < \hat{\theta}_i < \theta_{i\,max}\right] \\ & \text{or } \left[\hat{\theta}_i = \theta_{i\,max} \text{ and } \gamma\,(Y\,s_\epsilon)_i \geq 0\right] \\ & \text{or } \left[\hat{\theta}_i = \theta_{i\,max} \text{ and } \gamma\,(Y\,s_\epsilon)_i \leq 0\right] \\ 0, & \text{if } \left[\hat{\theta}_i = \theta_{i\,min} \text{ and } \gamma\,(Y\,s_\epsilon) > 0\right] \end{cases} \tag{6.14}$$

In a similar way operator Proj $\left(\hat{\phi}, -\eta\, u_{fd}\, \mathbf{s}_\epsilon\right)$ is:

$$Proj\left(\hat{\phi}, -\eta\, u_{fd}\, \mathbf{s}_\epsilon\right) = \begin{cases} 0, & \text{if} \left[\hat{\phi}_i = \phi_{i\,max} \text{ and } -\eta\, u_{fd}\, \mathbf{s}_\epsilon < 0\right] \\ -\eta\, u_{fd}\, \mathbf{s}_\epsilon, & \text{if} \left[\phi_{i\,min} < \hat{\phi}_i < \phi_{i\,max}\right] \\ & \text{or} \left[\hat{\phi}_i = \phi_{i\,max} \text{ and } -\eta\, u_{fd}\, \mathbf{s}_\epsilon \geq 0\right] \\ & \text{or} \left[\hat{\phi}_i = \phi_{i\,max} \text{ and } -\eta\, u_{fd}\, \mathbf{s}_\epsilon \leq 0\right] \\ 0, & \text{if} \left[\hat{\phi}_i = \phi_{i\,min} \text{ and } -\eta\, u_{fd}\, \mathbf{s}_\epsilon > 0\right] \end{cases} \tag{6.15}$$

6.2.2.3 Choice of design parameters

Choice of ϵ Parameter ϵ defines the saturation function and can principally be chosen freely without any constraints. But if it becomes too small, the linear region defined by $\mathbf{s}/\epsilon$ (See Figure 6.8) will be even smaller and chattering phenomena are very likely. This inhibits somehow a trade-off between small but still large enough to avoid chattering. For implementations, ϵ was chosen around $\epsilon \approx 0.01$.

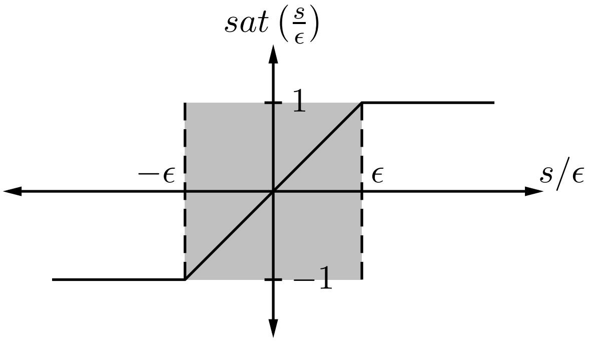

Figure 6.8: Saturation function with the linear area defined by $\mathbf{s}/\epsilon$

Choice of γ, η The two parameters γ and η determine the adaption time of the Proj.-operators. As the initial values for both θ and ϕ seem to be well known, no fast adaption is necessary. A good value around ≈ 0.5 turned out to be a good choice.

Choice of k_s k_s is one of the control gains and is mostly used to compensate the hysteresis bound $d(v)$. Therefore k_s should fulfil $k_s \geq \rho/a_{min}$, where ρ is given in (6.6) above. With $\rho = 7.72 \times 10^{-8}$ and $a_{min} = 1.6 \times 10^{-8}$ the resulting gain is $k_s = 4.82$.

Choice of k_d Another control gain is k_d which assesses the filtered tracking error. No certain constraints are given for this but fine tuning should be done experimentally. A gain with adequate tracking performance was found somewhere around $k_d \approx 30$.

Choice of λ Concerning the design parameter λ given in (6.8) no special calculation specification is given. In practice this means fine tuning is done experimentally. To get an idea of the size of λ, analysis of the mechanical system can obtain various factors limiting the parameter λ. In general three different factors are taken into consideration [29]:

- **Resonant mode:** λ should be lower than the lowest un-modelled resonance frequency f_R.

$$\lambda \leq \lambda_R \approx \frac{2\pi}{3} f_R \tag{6.16}$$

- **Neglected time delay:** Similar to above, the lowest un-modelled time delay (e.g. in some of the actuators or sensors) limits λ as follows:

$$\lambda \leq \lambda_D \approx \frac{1}{3T_D} \tag{6.17}$$

- **Sampling rate:** The sampling rate of the system defines another upper border for λ:

$$\lambda \leq \lambda_S \approx \frac{1}{5T_S} \tag{6.18}$$

λ appears then to be the minimum of the three upper limits $\lambda_R, \lambda_D, \lambda_S$. Equation (6.16) accounts on the mechanical properties, whereas (6.17) reflects the time delays and (6.18) depends on the sampling time. For the system in account this leads to the following limitations:

$$\lambda_R = 7129 \qquad \lambda_D = \text{not specified} \qquad \lambda_S = 2000 \tag{6.19}$$

For final implementations λ was chosen around 1500.

The summarized design parameters for the applied adaptive control are listed again in Table 6.4. As some values are ascertained experimentally, this listing does not claim perfect tuned values but rather gives a good possibility of choice.

ϵ	γ	η	k_s	k_d	λ
0.01	0.5	0.5	4.82	30	1500

Table 6.4: Design parameters for the adaptive controller

6.2.3 Simulation results

The controller was tested in simulation for a triangle signal at diverse amplitudes and frequencies. For all tests promising results were attained. Figure 6.9 shows the desired trajectory and the real displacement respectively.

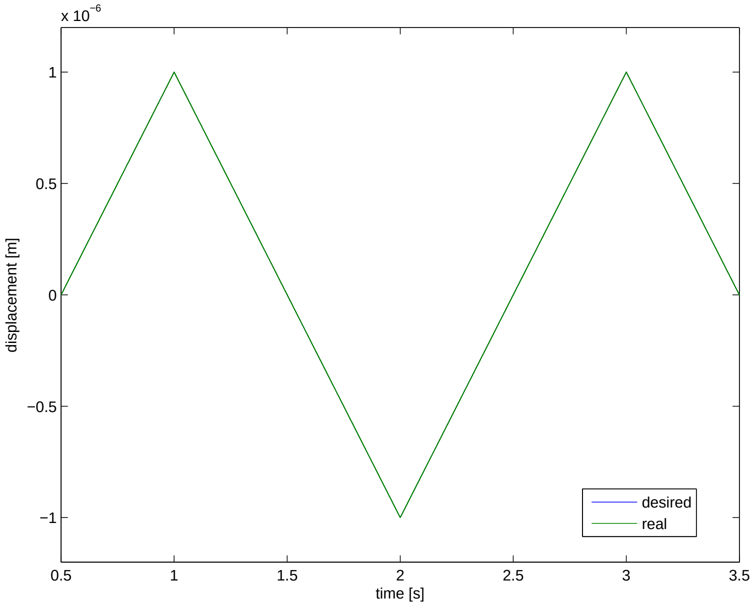

Figure 6.9: Tracking performance of the adaptive controller for ±1μm at 5 Hz

Chapter 7

Evaluation

> Niemals geht man so ganz, irgendwas von mir bleibt hier.
>
> Trude Herr

7.1 Summary of results, Conclusions

The main focus of this thesis was the improvement of resolution for a PZT actuator setup. This can be done either way on the mechanical and electrical side.

The mechanical design was slightly changed and adapted to the latest perceptions. In a preceding work [32] some problems concerning a too low resonance frequency turned up. The reasons for that were the rather compliable plastic fixture of the PZT and the heavy brass cube on the top of the tube. This has been rebuilt with a much lighter aluminium cube and another aluminium disc at the bottom. These upgrades raised the first resonance frequency to a frequency approx. 3 times higher than in [32]. Regarding vibrational damping, a rubber elastic board (as used in [32]) was replaced by a new air dampened table which ensures better vibrational damping from external sources.

The second and main part of this thesis covered the topic of a Kalman filter implementation to gain the PZT displacement resolution. Needed for such an implementation is a system description, most likely in state space form so as to integrate the Kalman filter in a most convenient way. In the course of this work, at first the individual partial models of the amplifier, capacitance and strain sensors, piezoelectric tube, hysteresis effects and creep effects were presented and then combined to a total system. Stressed out at this point should be the excellent compliance between the mechanical model (based on physical relations) and the measured one. This indicates the succeeding improvements done on the mechanical side of the lab setup. Two different PZT systems were investigated. At first a linear model was presented, and based on this model the linear Kalman filter was designed. A number of experiments obtain excellent estimation of the tube's displacement. Furthermore a state space controller concluded the work with the linear model. With this the appearing fluctuations at higher frequencies were successfully decreased.

In a second step the nonlinear system model was designed. For this the hysteresis effects of the PZT were incorporated and another extended model has been presented. Two different hysteresis models were presented, where [9] suggested a suitable model description. Parameters for this model were both approximated and calculated by means of an RLS algorithm. Due to nonlinearities, the previous linear Kalman filter could not be used anymore. An extended Kalman filter tackled the new system. Also with this implementation satisfying results were attained. Eventually a robust controller developed on the nonlinear model should care for the requisite tracking. Unfortunately this was simulated only and not tested with the real hardware. But still promising simulations show a well-operating system combining the estimation and control issues.

7.2 Further work

Although the results given in the preceding chapters are quite satisfactory, several improvements can be suggested. By providing an even more detailed system model, the Kalman filter performance can be raised to a next level. In details a higher order mechanical model, creep effects (as presented in Section 3.4), cross correlations or additional sensors should be discussed. Furthermore the controller schemes presented within Chapter 6 were a rather coarse approach. Especially the robust controller can be modified and should be tested under real conditions. Many different articles dealt with this topic and the presented results promise further improvements concerning the resolution. Another topic of further investigations is the cross correlation. Influences on that have not been part of this thesis and need to be analysed . This could be a next step for further research.

Bibliography

[1] W. Heerens A. E. Holman, P. Scholte and F. Tuinstra. Analysis of piezo actuators in translation constructions. *Review of Instruments, AIP*, 66:pp. 3208–3215, 1995.

[2] A.J. Fleming B. Bhikkaji, M. Ratnam and R. Moheimani. High performance control of piezoelectric tube scanners. *IEEE Transactions on control systems technology*, 15(5):pp. 853–866, 2007.

[3] R. Bauer. *Zustandsschätzung und Filterung, Lecture Notes*. Institute of Automation and Control, TU Graz, 2008.

[4] K.S. Birdi. *Scanning Probe Microscopes, Applications in Science and Technology*. CRC Press, 2007.

[5] R.G. Brown and P.Y.C. Hwang. *Introduction to random signals and applied kalman filtering*. John Wiley and Sons, 1997.

[6] K.J. Astrom C. d. Wit, H. Olsson and P. Lischinsky. A new model for control of systems with friction. *IEEE Transaction on automatic control*, 40(3):pp. 419–425, 1995.

[7] J. Svoboda C-Y. Su, Y. Stepanenko and T.P. Leung. Robust adaptive control of a class of nonlinear systems with unknown backlash-like hysteresis. *IEEE Transactions on automatic control*, 45(12):pp. 2427–2432, 2000.

[8] J. Chen. *Introduction to Scanning Tunneling Microscopy*. Oxford University Press, 1993.

[9] B.D. Coleman and M.L. Hodgdon. A constitutive relation for rate independent hysteresis in ferromegnetically soft materials. *International journal of engineering science*, 24(6):pp. 897–919, 1986.

[10] S.H. Crandall. *An Introduction to the Mechanics of Solids*. McGraw-Hill, 1978.

[11] G. Shed D. Croft and S. Devasia. Creep, hysteresis and vibration compensation for piezoactuators: Atomic force microscopy application. *Journal of Dynamic Systems, Measurement and Control*, 123:pp. 35–43, 2001.

[12] O. Egeland and J.T. Gravdahl. *Modeling and Simulation for Automatic Control*. Marine Cybernetics, 2002.

[13] A.J. Fleming and R. Moheimani. Improved current and charge amplifiers for driving piezoelectric loads. *Journal of Intelligent Material Systems and Structures*, 15(2):pp. 77–92, 2004.

[14] C.F. Quate G. Binnig and C. Gerber. Atomic force microscope. *Physical Review Letters*, 56(3):pp. 930–934, 1985.

[15] G. Gautschi. *Piezoelectric Sensorics*. Springer, 2002.

[16] M.S. Grewal and A.P. Andrews. *Kalman Filtering, Theory and Practice Using MATLAB*. John Wiley and Sons, 2001.

[17] D. Helmick and W. Messner. Higher order modeling of hysteresis in disk drive actuators. *Proceedings of IEEE conference on decision and control*, 42:pp. 3712–3716, 2003.

[18] R. Banning H.J. Adriaens, W.L.d. Koning and K.R. Koops. State space analysis and identification for a class of hysteresis systems. *Automatica*, 37:pp. 1883–1892, 2001.

[19] W.L.d. Koning H.J. Adriaens and R. Banning. Modeling piezoelectric actuators. *IEEE/ASME Transaction on Mechatronics*, 5(4):pp. 331–341, 2000.

[20] M. Horn and N. Dourdoumas. *Regelungstechnik*. Pearson Studium, 2004.

[21] A.J. Fleming J. Maess and F. Allgoewer. Simulation of piezoelectric tube actuators by reduced finite element models for controller design. *American Control Conference*, pages pp. 4221–4226, 2007.

[22] S. Buchner L. P. Fowler and V. Ryaboy. Self-contained active damping system for pneumatic isolation tables. *Industrial and commercial applications of smart structures technologies. Conference, Newport Beach,*, 3991:pp. 261–272, 2000.

[23] G. Moschytz and M. Hofbauer. *Adaptive Filter*. Springer, 2000.

[24] C.V. Newcomb and I. Flinn. Improving the linearity of piezoelectric ceramic actuators. *Electronics Letters*, 18(11):pp. 442–444, 1982.

[25] T. Ohara and K. Youcef-Toumi. Dynamics and control of piezotube actuators for subnanometer precision applications. *American control conference*, 5:pp. 3808–3812, 1995.

[26] T. Ohara and K. Youcef-Toumi. Coupling in piezoelectric tube scanners used in scanning probemicroscopes. *American control conference*, 4:pp. 3251–3255, 2001.

[27] T. Ohara and K. Youcef-Toumi. Modeling of piezoelectric tube actuators. *DSpace@MIT*, pages pp. 1–8, 2004.

[28] J. Sirohi and I. Chopra. Fundamental understanding of piezoelectric strain sensors. *Journal of Intelligent Material Systems and Structures*, 11(4):pp. 246–257, 2000.

[29] J-J.E. Slotine and W. Li. *Applied nonlinear Control.* Prentice Hall, 1991.

[30] Y. Stepanenko and C-Y. Su. Intelligent control of piezoelectric actuators. *Proceedings of IEEE conference on decision and control*, 4:pp. 4234–4239, 1998.

[31] U. Tietze and Ch. Schenk. *Halbleiter-Schaltungstechnik*, volume 13. Springer, 2010.

[32] E. Vinge. Nanopositioning, construction and analysis of a piezoelectric tube actuator. Master's thesis, NTNU Trondheim, 2009.

[33] R. Wiesendanger. *Scanning Probe Microscopy and Spectroscopy, Methods and Applications.* Cambridge University Press, 1994.

Appendix A

IFAC Abstract

At the department of cybernetics at NTNU a paper on tracking control for piezoelectric nanopositioners was suggested for the IFAC Symposium on Mechatronic Systems 2010 and the ASME Dynamic Systems and Control Conference 2010. This paper was partly inspired by this thesis. An abstract can be found in the following.

Tracking Control for a Piezoelectric Nanopositioner using Estimated States and Feed-forward Compensation of Hysteresis

Arnfinn Aas Eielsen (eielsen@itk.ntnu.no)
Lukas Vogl (vogl@stud.ntnu.no)
Jan Tommy Gravdahl (Jan.Tommy.Gravdahl@itk.ntnu.no)
Kristin Y. Pettersen (Kristin.Ytterstad.Pettersen@itk.ntnu.no)

Department of Engineering Cybernetics
Norwegian University of Science and Technology
7491 Trondheim, Norway

Nanopositioning stages utilizing piezoelectric actuators exhibit several undesired features inhibiting good reference tracking performance. The most salient features are lightly damped mechanical resonances, hysteresis, and creep. In addition, sensor noise limits the resolution achievable when applying closed-loop control schemes.

In order to improve the precision, and for sensor fusion, when using closed-loop control, we develop a non-linear state estimator using the extended Kalman filter. Furthermore we propose a novel method for compensating the hysteric behavior in piezoelectric actuators when tracking a reference trajectory, and present a method for online identification of the parameters of the system, aiming for simplicity and ease of implementation. The backstepping framework is used to obtain an adaptive control law and to analyze stability and boundedness of the tracking error.

Experimental results are presented in order to assess the performance of the proposed control scheme on a flexure-based nanopositioner using piezoelectric actuators.

Appendix B

Zero offset circuit

Charge measurement signals often have some undesirable offsets. To get rid of them, a circuitry to automatically detect the offset is presented in the following.

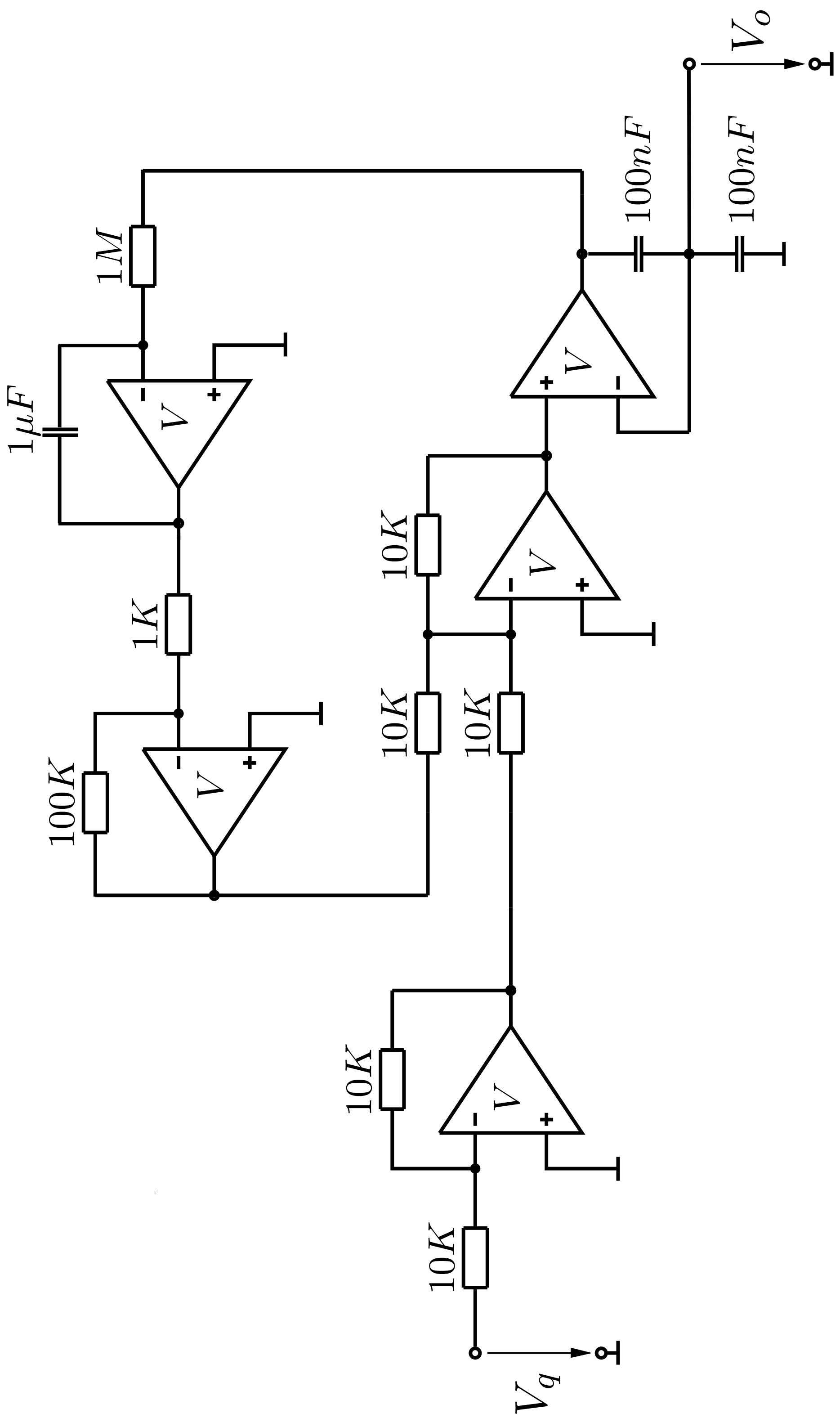
V_o
100nF
100nF
1M
1μF
V
V
V
V
V
1K
100K
10K
10K
10K
10K
10K
V_q

Deutsche Fassung:
Beschluss der Curricula-Kommission für Bachelor-, Master- und Diplomstudien vom 10.11.2008
Genehmigung des Senates am 1.12.2008

EIDESSTATTLICHE ERKLÄRUNG

Ich erkläre an Eides statt, dass ich die vorliegende Arbeit selbstständig verfasst, andere als die angegebenen Quellen/Hilfsmittel nicht benutzt, und die den benutzten Quellen wörtlich und inhaltlich entnommenen Stellen als solche kenntlich gemacht habe.

Graz, am …………………………… ………………………………………………..
(Unterschrift)

Englische Fassung:

STATUTORY DECLARATION

I declare that I have authored this thesis independently, that I have not used other than the declared sources / resources, and that I have explicitly marked all material which has been quoted either literally or by content from the used sources.

…………………………… ………………………………………………..
date (signature)